Magma mixing during conduit flow is reflected in melt-inclusion data from persistently degassing volcanoes

Zihan Wei[1,1], Zhipeng Qin[2,2], and Jenny Suckale[1,1]

[1]Stanford University
[2]Guangxi University

March 21, 2023

Abstract

Persistent volcanic activity is thought to be linked to degassing, but volatile transport at depth cannot be observed directly. Instead, we rely on indirect constraints such as CO2-H2O concentrations in melt inclusions trapped at different depth, but this data is rarely straight-forward to interpret. In this study, we develop a multiscale model of conduit flow during passive degassing to identify how flow behavior in the conduit is reflected in melt-inclusion data and surface gas flux. During the approximately steady flow likely characteristic of passive-degassing episodes, variability in degassing arises primarily from two processes, the mixing of volatile-poor and volatile-rich magma and variations in CO2 influx from depth. To quantify how conduit-flow conditions alter mixing efficiency, we first model bidirectional flow in a conduit segment at the scale of tens of meters while fully resolving the ascent dynamics of intermediate-size bubbles at the scale of centimeters. We focus specifically on intermediate-size bubbles, because these are small enough not to generate explosive behavior, but large enough to alter the degree of magma mixing. We then use a system-scale volatile-concentration model to evaluate the joint effect of magma mixing and CO2 influx on volatile concentrations profiles against observations for Stromboli and Mount Erebus. We find that the two processes have distinct observational signatures, suggesting that tracking them jointly could help identify changes in conduit flow and advance our understanding of eruptive regimes.

Magma mixing during conduit flow is reflected in melt-inclusion data from persistently degassing volcanoes

Zihan Wei[1], Zhipeng Qin[2], Jenny Suckale[1]

[1]Department of Geophysics, Stanford University, Stanford, CA, USA
[2]School of Mechanical Engineering, Guangxi University, Nanning, Guangxi, 53004, PR China

Key Points:

- Magma mixing occurs commonly at the interface between volatile-rich and volatile-poor magma in persistently degassing volcanoes
- Bubble speed, magma viscosities, and bubble volume fraction control magma mixing
- Magma mixing and carbon dioxide fluxing leave distinct signatures in melt-inclusion data

Corresponding author: Zihan Wei, zihanwei@stanford.edu

Abstract

Persistent volcanic activity is thought to be linked to degassing, but volatile transport at depth cannot be observed directly. Instead, we rely on indirect constraints such as CO_2-H_2O concentrations in melt inclusions trapped at different depth, but this data is rarely straight-forward to interpret. In this study, we integrate a multiscale conduit-flow model for non-eruptive conditions and a volatile-concentration model to compute synthetic profiles of volatile concentrations for different flow conditions and CO_2 fluxing. We find that actively segregating bubbles in the flow enhance the mixing of volatile-poor and volatile-rich magma in vertical conduit segments, even if the radius of these bubbles is several orders of magnitude smaller than the width of the conduit. This finding suggests that magma mixing is common in volcanic systems when magma viscosities are low enough to allow for bubble segregation as born out by our comparison with melt-inclusion data: Our simulations show that even a small degree of mixing leads to volatile concentration profiles that are much more comparable to observations than either open- or closed-system degassing trends for both Stromboli and Mount Erebus. Our results also show that two of the main processes affecting observed volatile concentrations, magma mixing and CO_2 fluxing, leave distinct observational signatures, suggesting that tracking them jointly could help better constrain changes in conduit flow. We argue that disaggregating melt-inclusion data based on the eruptive behavior at the time could advance our understanding of how conduit flow changes with eruptive regimes.

Plain Language Summary

Persistently degassing volcanoes typically erupt multiple times a day, emitting copious gas and thermal energy but relatively little magma. The ascent of the erupted magma is likely a byproduct of degassing, but it is unclear how exactly eruptive behavior and degassing are related. Without the ability to observe degassing processes at depth, we rely on erupted samples to derive constraints on pre-eruptive flow conditions. Some of these samples seal in magma droplets named melt inclusions, which represent valuable snapshots of volatile concentrations at depth. Here, we use numerical simulations to study how magma flow in vertical conduit segments at depth alters the volatile concentrations in melt inclusions. We demonstrate that volatile-rich, ascending magma mixes with volatile-poor, descending magma that has lost volatiles at the surface. The degree of mixing depends on the physical properties of magma and bubbles. This magma mixing, together with the carbon dioxide fluxing, can significantly shift the water and carbon dioxide concentrations in melt inclusions. Our study suggests that some degree of magma mixing is almost inevitable in persistently degassing volcanoes, but that mixing may vary considerably with depth. We suggest that melt-inclusion data could potentially help tracking the evolving flow conditions in volcanic conduits.

1 Introduction

Measurements of surface gas fluxes show that persistently degassing volcanoes continually emit copious quantities of gas and thermal energy, but rarely erupt large volumes of magma (Stoiber & Williams, 1986; Allard et al., 1994; Kazahaya et al., 1994; Palma et al., 2008; Oppenheimer et al., 2009; Woitischek et al., 2020). This imbalance suggests that much more magma is being degassed than erupted. One way of reconciling magma and gas transport is bidirectional flow that – akin to a conveyor belt – transports volatile-rich magma close to the surface where it degases and then sinks back down to depth having lost its buoyant cargo (Francis et al., 1993; Kazahaya et al., 1994). The most common configuration for bidirectional flow in vertical or near-vertical pipes is core-annular flow (Stevenson & Blake, 1998; Huppert & Hallworth, 2007; Beckett et al., 2011) with volatile-rich, less viscous magma ascending in the center of the conduit and volatile-poor, more viscous magma descending along the sides of the conduit in the form of a viscous annulus.

The concept of bidirectional flow is appealing from a theoretical point of view, because it provides the significant thermal energy flux required to maintain open-system conditions in persistently degassing volcanoes. Evaluating it from an observational point of view, however, is complicated by the inability to observe conduit flow directly. Nonetheless, several pieces of indirect evidence exist. For Kīlauea volcano, these include measured volatile concentrations in tholeiitic glasses (Dixon et al., 1991), a large proportion of misaligned olivine crystals erupted in 1959 (DiBenedetto et al., 2020), and direct observations of backflow (Eaton et al., 1987). At Erebus volcano, oscillatory zoning in megacrystals (Moussallam et al., 2015) have been interpreted as indications of bidirectional flow. There is also textural evidence from an exhumed mafic conduit that seems to suggest active bidirectional flow in the past (Wadsworth et al., 2015).

However, most of these pieces of evidence refer to a specific volcanic system, and sometimes even to a specific eruption. If the flow field in conduit segments at many or most persistently degassing volcanoes can be approximated as bidirectional flow, then it should have left an imprint that is more broadly detectable. Identifying this potential imprint would be particularly valuable during non-eruptive phases, because the majority of degassing observations occurs during approximately steady conditions characterized mostly by gas escaping passively from the volcanic conduit (e.g., Burton et al., 2007a; Oppenheimer et al., 2009; Ruth et al., 2018), but requires linking conduit flow conditions and degassing processes directly.

Some erupted samples can be used to reconstruct the degassing processes during non-eruptive conditions, because they may contain host crystals that have entrapped small droplets of melts during their growth (e.g., Métrich et al., 2001, 2010; Oppenheimer et al., 2011; Rasmussen et al., 2017). These melt inclusions are sealed in at various depth and thus represent valuable snapshots of evolving melt compositions (Ruth et al., 2018). Patching together these snapshots to obtain a consistent picture of degassing at depth, however, is hindered by the limited fidelity with which melt-inclusion seal in pre-eruptive conditions at depth (Bucholz et al., 2013; Aster et al., 2016; Barth et al., 2019) and measurement uncertainty (Oppenheimer et al., 2011). Another important observable that helps to constrain steady degassing is the surface-gas flux (Burton et al., 2007a; Oppenheimer et al., 2009; Ilanko et al., 2015). Surface-gas-flux measurements provide an important complement to melt-inclusion data, because melt inclusions only seal melt and are unsuitable for estimating the total budgets of volatiles with low solubility, such as CO_2 (e.g., Wallace, 2005; Burton et al., 2007b)

The goal of this study is to quantify how different rates of magma mixing in conduit flow and variations in CO_2 fluxing alter the volatile concentrations recorded by melt-inclusions during non-eruptive conditions. We hypothesize that CO_2 fluxing (Burton et al., 2007b; Blundy et al., 2010; Métrich et al., 2010; Rasmussen et al., 2017) and magma mixing (Witham, 2011a; Moussallam et al., 2016) leave distinct signatures in melt-inclusion data. Identifying these distinct observational signatures would allow distinguishing between the relative importance of the two processes during conduit flow and potentially afford new insights into their relationship with eruptive behavior. Spilliaert et al. (2006) provided a proof-of-concept of this idea, but without integrating a magma dynamics model.

To connect conduit flow to melt-inclusion data, we link a multiscale model of bidirectional conduit flow to a volatile-concentration model. The conduit-flow model is multiscale in the sense that it resolves both the flow dynamics of a conduit segment at the tens-of-meter scale and the ascent dynamics of bubbles through a direct numerical approach (Qin & Suckale, 2017; Suckale et al., 2018; Qin et al., 2020). We only resolve actively segregating bubbles that are buoyant enough to decouple from the magmatic liquid and ascend, but not so large that they might be related to eruptive behavior (e.g., Jaupart & Vergniolle, 1988). Very small crystals and bubbles have much smaller ascent speeds than the magmatic liquid and hence remain largely entrained (Tryggvason et al., 2013). As a consequence, their main effect is to alter the effective material properties of the bubble-crystal-melt mixture (Bowen, 1976).

With our conduit-flow model, we analyze how actively segregating bubbles perturb the interface between volatile-rich and volatile-poor magma and create magma mixing. Previous studies demonstrate that in the absence of small bubbles or crystals, the interface is stable for two miscible magmas with low diffusivity and sufficiently high viscosity contrast (Stevenson & Blake, 1998; Suckale et al., 2018). The presence of bubbles and crystals might change that because hydrodynamic interactions between them create spatial correlations in velocity even at very low phase fractions of a few percent (Segre et al., 1997, 2001). The effect of these hydrodynamic correlations on flows at low Reynolds number is reminiscent of the effect of turbulence on flows at high Reynolds number (Xue et al., 1992; Tong & Ackerson, 1998; Levine et al., 1998). In magmatic systems, mixing is hence dominated by multiphase interactions rather than turbulence. In that aspect, our model differs from Witham (2011a), who assumed turbulent mixing.

We test our hypothesis by comparing the volatile concentrations computed based on different degrees of magma mixing against the volatile concentrations recorded in melt inclusions. In our computations, we first quantify magma mixing with the conduit-flow model and then use the volatile-concentration model based on Witham (2011a) to calculate the associated system-scale concentration profiles. Regarding the comparison with observations, we focus specifically on Stromboli and Mount Erebus because of their abundance of melt-inclusion data (Métrich et al., 2010; Oppenheimer et al., 2011; Rasmussen et al., 2017), the availability of continuous measurements of surface gas fluxes (Burton et al., 2007a; Oppenheimer et al., 2009; Ilanko et al., 2015), and the relatively steady patterns of their degassing and eruption activities (Allard et al., 1994; Burton et al., 2007a; Oppenheimer et al., 2009, 2011; Métrich et al., 2010; Rasmussen et al., 2017).

A particularly puzzling observation is that melt inclusions from many persistently degassing volcanoes consistently indicate higher CO_2 content than predicted by either closed-system or open-system degassing path (Métrich & Wallace, 2008; Métrich et al., 2010; Blundy et al., 2010; Oppenheimer et al., 2011; Yoshimura, 2015; Rasmussen et al., 2017; Barth et al., 2019). In contrast, melt inclusions from more silicic volcanoes appear to match the expected trends more closely (e.g., Schmitt, 2001; Liu et al., 2006), suggesting that melt inclusions may at least partially reflect systematic differences in conduit flow between different volcanic systems. While CO_2 fluxing (Burton et al., 2007b; Shinohara, 2008; Blundy et al., 2010; Métrich et al., 2010; Rasmussen et al., 2017) and magma mixing (Dixon et al., 1991; Witham, 2011a; Sides et al., 2014) are often presented as alternative explanations (Métrich et al., 2011; Witham, 2011b), we argue here that they both contribute to the observed variability in volatile concentrations, but do so in distinct ways.

2 Method

From individual bubbles and crystals to transcrustal plumbing systems (Cashman et al., 2017), volcanic systems bridge ten orders of magnitude in spatial scale or more (e.g., fig. 1). Fully resolving all physical and chemical processes over this vast spectrum of spatial scales at the accuracy necessary to understand the nonlinear dynamics of a highly coupled system is not possible. Rather than attempting to model plumbing-system dynamics in its full complexity, we focus on the element that dominates vertical transport, namely conduit-like segments that may exist at different depths. We develop a customized multiscale framework that focuses on the key elements required for linking bidirectional flow and observations of melt-inclusions and surface-gas flux in vertical conduit segments. This framework consists of two main components, the conduit-flow model and the volatile-

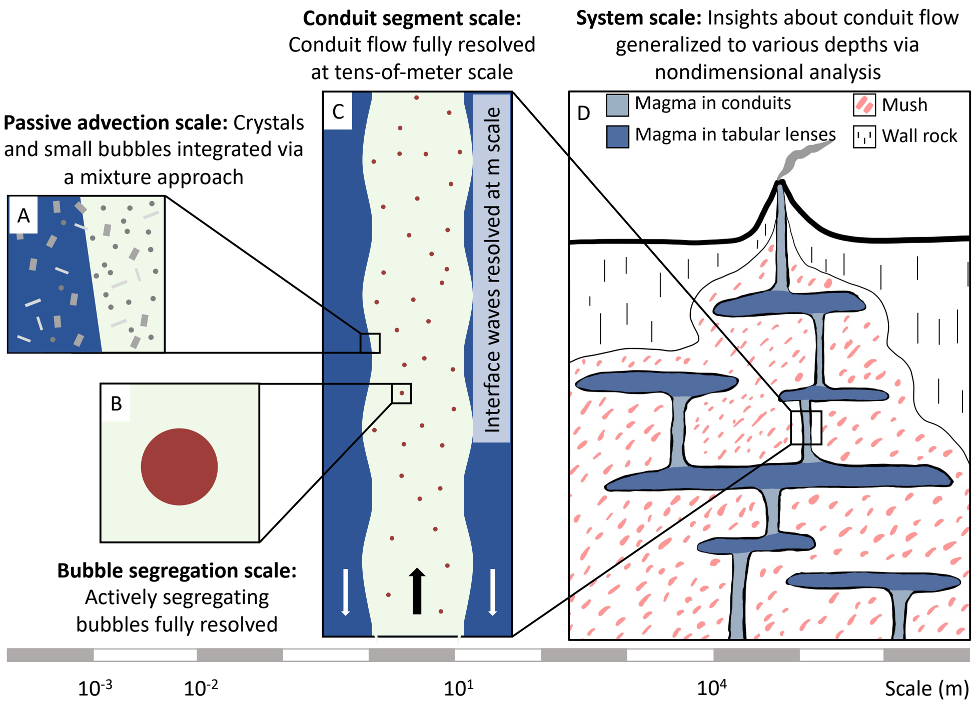

Figure 1. Overview of relevant spatial scales in volcanic systems and their model representation.

concentration model, described in more detail in the next two sections. Table 1 lists the definitions and units of all symbols.

2.1 Conduit-flow Model

Transcrustal plumbing system (Cashman et al., 2017; Magee et al., 2018) consists of vertically stacked melt-rich tabular lenses and vertical conduit-like segments connecting these lenses at least transiently (see fig. 1D). While magma properties, such as gas volume fraction and melt viscosity, can vary significantly over the entirety of this system, we assume that they are approximately constant at the scale of small conduit-like segments that are a few times the conduit radius in lengths and hence typically a few meters to tens of meters long (fig. 1C). This assumption implies that crystallization, exsolution and dissolution are negligible within these segments.

We assume that flow in the vertical, conduit-like segments is driven by buoyancy. Volatiles exsolved at depth provide the buoyancy required for the ascent of volatile-rich magma. Upon degassing at the free surface, volatile-poor magma remains and sinks back to depth, creating a bidirectional flow field (Blake & Campbell, 1986; Francis et al., 1993; Kazahaya et al., 1994; Stevenson & Blake, 1998; Molina et al., 2012). More specifically, we assume a core-annular flow geometry, because it is the most commonly observed configuration in vertical, or near-vertical, pipes at moderate to high viscosity contrasts (Stevenson & Blake, 1998; Huppert & Hallworth, 2007; Beckett et al., 2011).

In conduit segments, bubbles segregate from the ambient magma flow and rise towards the surface to degas. According to Stokes' law, the bubble rise speed scales with r^2, where r is the bubble radius. Larger bubbles hence segregate much more efficiently than smaller bubbles. We capture the actively segregating bubbles explicitly using direct numerical simulations (fig. 1B). We assume that crystals and very small bubbles,

Table 1. Definitions and units of parameters and variables, and values of constants

	Unit	Definition	Value
Conduit-flow model:			
c		concentration variable representing the content of dissolved volatile and passively advecting bubbles	
ΔC_{H_2O}		difference in the weight percent of dissolved H_2O in volatile-rich and volatile-poor magma	
D	m^2/s	diffusion coefficient	10^{-10}
D_H	m^2/s	hydrodynamic diffusion coefficient	
$\mathbf{F}_b$	N	hydrodynamic force exerted onto the bubble	
g	m/s^2	gravitational acceleration	9.81
L	m	conduit length	21
M		viscosity contrast (μ_p/μ_r)	
M_b	kg	mass of a bubble	
p	Pa	pressure	
P		nondimensional driving force	
δp	Pa	approximate pressure drop through the domain	
r	m	bubble radius	
R	m	conduit radius	1.5
Sc		Schmidt Number	
t	s	time	
$\hat{t}$		nondimensional time	
U	m/s	characteristic speed of the analytical solution	
$\mathbf{v}$	m/s	velocity	
v_b	m/s	Stokes rise speed	
v_c	m/s	vertical speed at the center line of the analytical solution	
$\mathbf{V}_b$	m/s	bubble velocity	
$\mathbf{X}_b$	m	the position of the center of mass of a bubble	
Γ		mixing factor	
δ		interface location of the analytical solution	0.54
μ	Pa·s	magma viscosity	
μ_p	Pa·s	viscosity of volatile-poor magma	
μ_r	Pa·s	viscosity of volatile-rich magma	
ρ	kg/m^3	magma density	
ρ_b	kg/m^3	density of bubbles	
ρ_p	kg/m^3	density of volatile-poor magma	
ρ_r	kg/m^3	density of volatile-rich magma	
σ		error of mixing factor	
τ_{xy}	Pa	simulated shear stress	
τ	Pa	analytical interfacial shear stress	
ϕ		volume fraction of actively segregating bubbles in volatile-rich magma	
$\Delta\phi_p$		difference in the volume fraction of passively advecting bubbles in volatile-rich and volatile-poor magma	
Volatile-concentration Model:			
i_a		weight percent of dissolved volatiles in ascending magma	
i_d		weight percent of dissolved volatiles in descending magma	
i_{ga}		weight percent of exsolved volatiles in ascending magma	
i_{gd}		weight percent of exsolved volatiles in descending magma	
i_*		effective ascending volatile content	
P	Pa	pressure	
P_{min}	Pa	minimum pressure	
P_{max}	Pa	maximum pressure	
Δp	Pa	pressure step size	
θ		proportion of passively advecting bubbles in ascending gas	
λ		H_2O(wt%)/CO_2(wt%) in the gas phase at the surface	

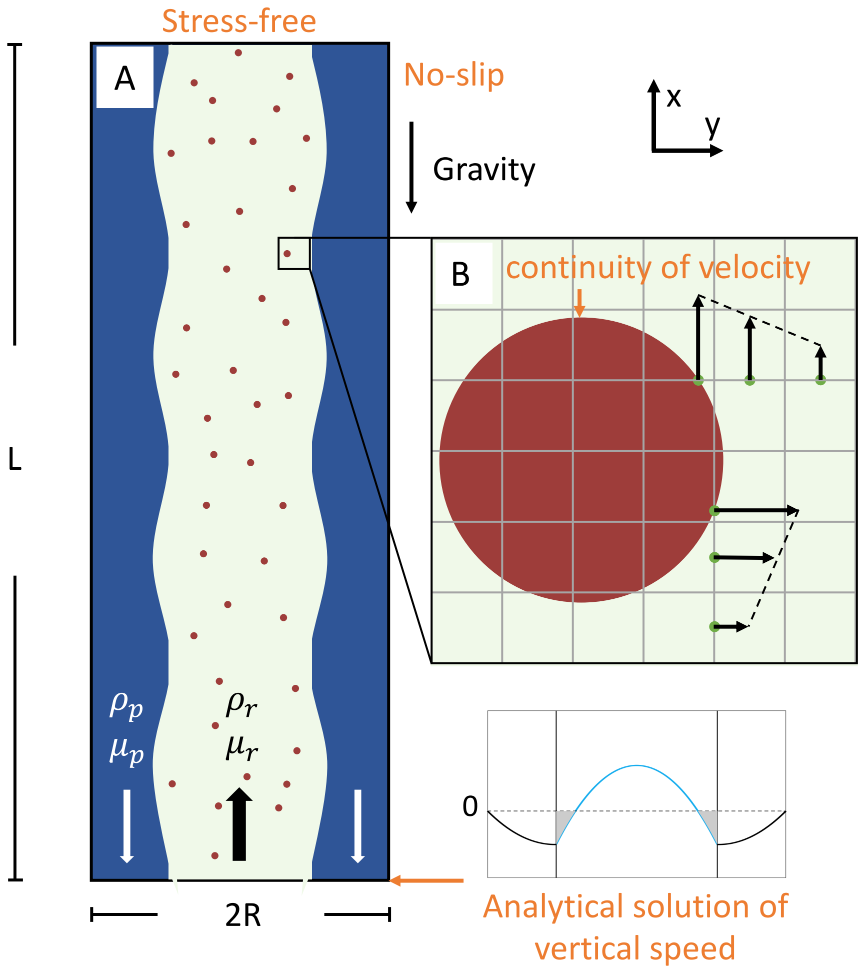

Figure 2. Illustration of the simulation domain of the conduit-flow model (not to scale). The orange text represents the boundary conditions. **(A)**: The model domain for simulating the conduit flow. In this study, $L = 21$m and $R = 1.5$m. **(B)**: We enforce the continuity of velocity as the boundary condition at the bubble-magma interface by linearly interpolating the bubble velocity and magma velocity for magma grid cells adjacent to bubbles (see Qin and Suckale (2017) for details). Vertical and horizontal arrows represent vertical and horizontal velocity components, respectively. Figure (B) is modified from Qin and Suckale (2017).

which have much lower segregation speeds, remain entrained in the ambient magma flow. We represent them implicitly through a mixture approximation (Bowen, 1976) by assuming that they passively advect with the magma and only affect the effective density and viscosity of the magma (fig. 1A). Hereafter, we use the term “magma” to refer to the mixture of melt and passively advecting bubbles and crystals. Resolving the flow around actively segregating bubbles while representing passively advecting bubbles and crystals through a subgrid mixture model is a commonly used approach in multiphase modeling as reviewed in Tryggvason et al. (2013).

The first step of our analysis is to quantify magma mixing via the multiscale conduit-flow model (fig. 2). The multiscale approach described above reduces our model to three distinct phases: (1) the volatile-rich, ascending magma, (2) the volatile-poor, descending magma and (3) actively segregating bubbles, contained mostly in the ascending flow. The viscosities for both magmas in our model are informed by previously estimated ranges for Stromboli (Burton et al., 2007b) and Mount Erebus (Sweeney et al., 2008). Since our model focuses on approximately steady flow during non-eruptive conditions, we do not consider the potential presence of large bubbles or slugs, because these are related to eruptive processes (Jaupart & Vergniolle, 1988; Del Bello et al., 2012; Qin et al., 2018). Since our bubbles are not large enough to deform significantly, we model them as spherical in the interest of simplicity.

We define a 2D rectangular simulation domain (fig. 2A) to represent a conduit segment (fig. 1C). We apply a stress-free condition ($p=$ const., $\frac{\partial \mathbf{v}}{\partial x}=0$) at the top boundary to enable free outflow. The side walls are no-slip. At the base we impose the analytical solution of vertical speed in core-annular flow (Suckale et al., 2018). We assume that the two magmas are miscible Newtonian fluids differing in viscosity and density. Both viscosity and density depend on the total pressure, or depth, of the conduit segment. In a given volcanic system, they could be calculated from the magma composition, temperature and pressure. Here, we capture depth variability implicitly through the broadly varying parameters in table 2 to keep our analysis general. Our simulations then allow us to better understand the parameters that govern the degree of magma mixing in vertical conduit segments generally, irrespective of one particular volcanic system.

We assume that the volatile-rich magma is less viscous by 1 to 2 orders of magnitude because it contains higher concentration of dissolved H_2O and fewer crystals (Giordano et al., 2008; Lesher & Spera, 2015). The volatile-rich magma has lower density because both the dissolved H_2O (Lesher & Spera, 2015) and the entrained passively advecting bubbles reduce the effective density of magma (fig. 1). The values of $\max(\Delta\phi_p)$ listed in table 2 represent the difference in the volume fraction of passively advecting bubbles in volatile-rich and volatile-poor magma if their density difference were entirely caused by the difference in the amount of passively advecting bubbles. The values of $\max(\Delta C_{H_2O})$ listed in table 2 represent the difference in the weight percent of dissolved H_2O in volatile-rich and volatile-poor magma if their density difference were entirely caused by the difference in the amount of dissolved H_2O, assuming 1 wt% of dissolved H_2O decreases magma density by 50kg/m^3 (Lesher & Spera, 2015). In the simulations listed in table 2, the proportion of bubbles that are actively segregating ranges from 0 to 1. This broad range is consistent with the highly varied observed bubble size distributions (e.g., Lautze & Houghton, 2005, 2007; Bai et al., 2008). Low proportion of actively segregating bubbles can be a result of multiple bubble nucleation events (Toramaru, 2014) during gas exsolution without significant bubble growth, while high proportion can be a result of a single nucleation event followed by continuous bubble growth.

Our model solves for the mass and momentum balance in an incompressible core-annular flow at low Reynolds number (Qin & Suckale, 2017; Suckale et al., 2018; Qin et al., 2020). The governing equations in the two magmas are the incompressibility condition

$$0 = \nabla \cdot \mathbf{v} \tag{1}$$

the Stokes equation,

$$0 = -\nabla p + \nabla \cdot (\mu \nabla \mathbf{v}) + \rho \mathbf{g}, \tag{2}$$

and the advection-diffusion equation for the concentration variable c to capture magma mixing

$$\frac{\partial c}{\partial t} + \mathbf{v} \cdot \nabla c = D \nabla^2 c, \tag{3}$$

where density, ρ, and viscosity, μ, are defined as

$$\rho = \begin{cases} \rho_p - c(\rho_p - \rho_r), & \text{in magma} \\ \rho_b, & \text{in bubbles} \end{cases}, \tag{4}$$

$$\mu = \mu_p - c(\mu_p - \mu_r), \tag{5}$$

p is pressure, $\mathbf{v}$ is velocity, and $\mathbf{g}$ is the gravitational acceleration. We compute the magmatic flow field on a Cartesian staggered grid with the finite difference method as described in detail by Qin and Suckale (2017). The nondimensional concentration variable c ranging from 0 to 1 represents the relative content of dissolved volatile, crystals, and passively advecting bubbles. The diffusion coefficient $D = 10^{-10}\mathrm{m}^2/\mathrm{s}$ refers to the diffusion of water in basaltic magma (Zhang & Stolper, 1991; Witham, 2011a). Initially, $c = 1$ in the volatile-rich magma and $c = 0$ in the volatile-poor magma. To present our simulation results, we define the contour of $c = 0.5$ as the interface between the two magmas. We assume that the density and viscosity of magma depend linearly on c, as shown in eqs. 4 and 5, where $\rho_r, \rho_p, \mu_r, \mu_p$ are the density and viscosity of the volatile-rich and volatile-poor magmas, respectively. In reality, the dependence is probably non-linear (Giordano et al., 2008), possibly exponential, which would translate into a more pronounced velocity contrast close to the interface (Suckale et al., 2018). The dynamics of the interface would be even more non-linear in this scenario, leading to potentially more mixing and unstable flow.

The 2D symmetric analytical solution of vertical speed derived in Suckale et al. (2018) imposed as the boundary condition at the base (fig. 2) is

$$v_x(y) = \begin{cases} U\left[\frac{P}{2}(\frac{y^2}{R^2} - 1) - \delta(\frac{y}{R} - 1)\right], & y \in [\delta R, R] \\ U\left[M\frac{P-1}{2}(\frac{y^2}{R^2} - \delta^2) + \frac{P}{2}(\delta^2 - 1) - \delta(\delta - 1)\right], & y \in [0, \delta R] \end{cases}, \tag{6}$$

where R is the conduit radius, $y = 0$ at the center and $y = R$ at the side walls, $\delta \in (0, 1)$ represents the location of the interface between the two magmas, $M = \mu_p/\mu_r$ is the viscosity contrast, P is the nondimensional driving force defined as

$$P = \delta\frac{3 + \delta^2(2M - 3)}{2 + 2\delta^3(M - 1)}, \tag{7}$$

and U is the characteristic speed defined as

$$U = (\rho_p - \rho_r)gR^2/\mu_p. \tag{8}$$

In all of our simulations, we impose the thick-core solution in Suckale et al. (2018) and set $\delta = 0.54$, because previous experiments have mostly observed thick-core flow (Stevenson & Blake, 1998; Huppert & Hallworth, 2007; Beckett et al., 2011).

Following Qin and Suckale (2017, 2020), and Qin et al. (2020), we describe actively segregating bubbles by the Newton's Laws of Motion

$$M_b\frac{d\mathbf{V}_b}{dt} = \mathbf{F}_b + M_b\mathbf{g}, \tag{9}$$

$$\frac{d\mathbf{X}_b}{dt} = \mathbf{V}_b, \tag{10}$$

where M_b is the mass of a bubble, $\mathbf{V}_b$ the bubble velocity, $\mathbf{F}_b$ the hydrodynamic force by the surrounding magma exerted onto the bubble, and $\mathbf{X}_b$ the position of its center of mass. As shown in fig. 2B, we enforce continuity of velocity at the bubble-magma interface by linearly interpolating the bubble velocity and magma velocity for magma grid cells adjacent to bubbles.

The numerical implementation (Wei et al., 2021) consists of three steps. The first step is solving eqs. 1 and 2. In this step, we slightly modify the numerical implementation of Qin and Suckale (2017, 2020), and Qin et al. (2020) by using the actual density of each phase to reduce the convergence steps instead of the liquid density for the entire domain. The second step is solving eq. 3 following Suckale et al. (2018). The third step is solving bubble motion following Qin and Suckale (2017, 2020), and Qin et al. (2020).

To quantify the magma mixing that occurs at the scale of a conduit segment, we define the mixing factor Γ ranging from 0 to 1 as the relative change in c associated with a pressure drop of $\Delta p = 1$MPa. To calculate Γ, we define c_b and c_t as the laterally averaged c in the ascending magma entering the domain from the bottom and leaving the domain from the top, respectively. We use the median value of $(c_b - c_t)/c_b$ over time as the estimated amount of mixing after the ascending magma moves through the domain. For a simulation with actively segregating bubble volume fraction ϕ, we approximate the pressure drop in this process analytically as $\delta p = gL[\rho_p + (1-\phi)\rho_r + \phi\rho_b]/2$, where L is the length of the conduit segment. Therefore, for each conduit flow simulation, we compute Γ and its associated error σ as

$$\begin{Bmatrix}\Gamma\\ \sigma\end{Bmatrix} = 1 - \left[1 - \begin{Bmatrix}\text{median}\\ \text{std}\end{Bmatrix}\left(\frac{c_b - c_t}{c_b}\right)\right]^{\frac{\Delta p}{\delta p}}. \tag{11}$$

While the simulated pressure field varies spatially and temporally, the error of the analytically approximated pressure drop is below 3% for all simulations in table 2.

2.2 Volatile-concentration Model

As a consequence of mixing, the ascending magma is gradually diluted as it ascends, while the descending magma becomes more volatile-rich as it descends. Using the estimated mixing factors from our simulations, we compute CO_2-H_2O concentration profiles at the system scale following Witham (2011a) with modifications (fig. 3; Wei et al., 2021). For both CO_2 and H_2O, we calculate the steady-state concentration profiles i_a, i_d, i_{ga}, and i_{gd} that represent the weight percent of dissolved volatiles in the ascending magma, dissolved volatiles in the descending magma, exsolved volatiles in the ascending magma, and exsolved volatiles in the descending magma, respectively. Witham (2011a) assumes that the descending magma is free of gas. According to our conduit-flow model, actively segregating bubbles that enter the descending magma in the conduit-flow model either return to the ascending magma quickly or continue ascending in the descending magma because of their own buoyancy (fig. 4G). However, passively advecting bubbles that enter the descending magma during mixing remain entrained. Contrary to Witham (2011a), we hence do not assume that the descending magma is free of gas, but instead track its the exsolved volatiles content, i_{gd}, in our model.

We illustrate the calculation of CO_2-H_2O concentration profiles in fig. 3. The pressure P ranges from $P_{min} = 1$ atm to P_{max} with a step size Δp. We set $i_a^{P_{max}} + i_{ga}^{P_{max}}$ as the composition of the most volatile-rich melt inclusions (Métrich et al., 2010; Oppenheimer et al., 2011), and set $P_{max} = 350$MPa based on the volatile solubility model MagmaSat (Gualda et al., 2012; Ghiorso & Gualda, 2015). We assume constant magma temperatures of 1180°C and 1000°C for Stromboli (Bertagnini et al., 2003; Métrich et al., 2010) and Mount Erebus (Kyle, 1977), respectively. We ignore crystallization and its influence on the solubility of volatiles, as done in previous studies (e.g., Métrich et al., 2010; Witham, 2011a; Rasmussen et al., 2017).

Following Witham (2011a), we initialize i_a and i_{ga} according to closed-system degassing. Then, we initialize the descending profiles by calculating

$$i_d^P = (1 - \Gamma)\, i_d^{P-\Delta p} + \Gamma i_a^P \tag{12}$$

and

$$i_{gd}^P = (1 - \Gamma)\, i_{gd}^{P-\Delta p} + \Gamma\theta i_{ga}^P \tag{13}$$

for the entire pressure range, where the superscripts indicate the pressure corresponding to the concentrations, and θ is proportion of passively advecting bubbles in the ascending gas. Eqs. 12 and 13 represent the transport of dissolved and exsolved volatiles from ascending magma to descending magma via mixing, respectively (fig. 3). At each pressure step, after calculating $i_d^P + i_{gd}^P$ using eqs. 12 and 13, we partition i_d^P and i_{gd}^P using MagmaSat (Gualda et al., 2012; Ghiorso & Gualda, 2015). At the surface, we assume all the exsolved volatiles escape and ascending magma starts to sink, thus $i_d^{P_{min}} =$

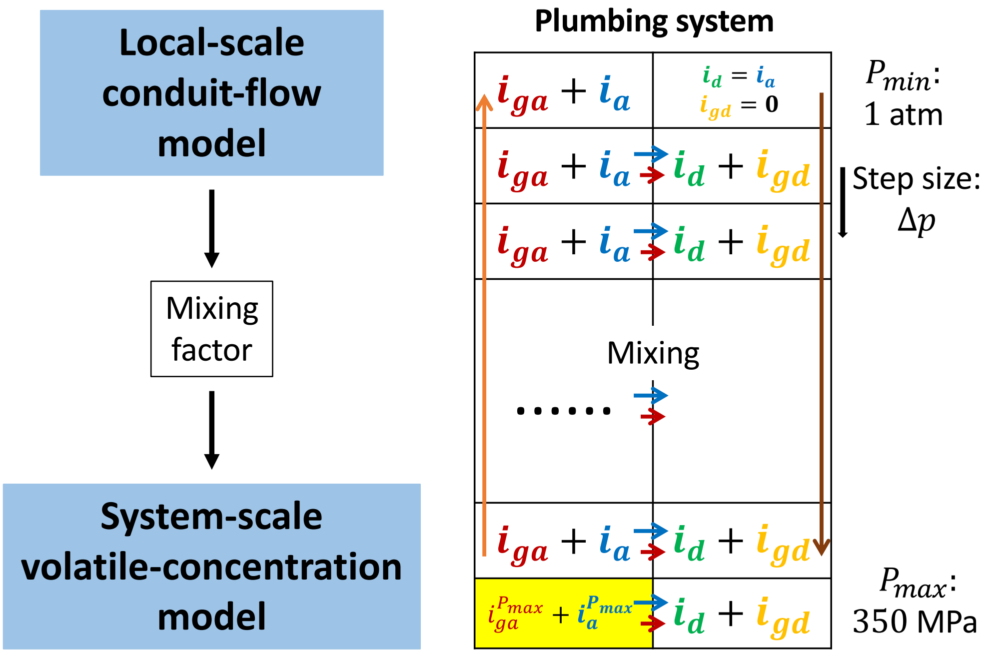

Figure 3. **Left**: workflow of our analysis. We summarize the simulation result of the conduit-flow model as a mixing factor, which is an input parameter for the system-scale volatile-concentration model. **Right**: Illustration of the volatile-concentration model. The left and right columns represent the ascending and descending magma, respectively. The lateral arrows represent the transport of dissolved and exsolved volatiles from ascending magma to descending magma via mixing at each pressure step. The yellow cell represents the fixed input set as the composition of the most volatile-rich melt inclusions.

$i_a^{P_{min}}$ and $i_{gd}^{P_{min}} = 0$ (fig. 3). Incorporating i_{gd} into the formulation by Witham (2011a), we defines the effective ascending concentration i_*^P as

$$\phi_u i_*^P = \phi_u \left(i_a^P + i_{ga}^P\right) - \phi_d \left(i_d^P + i_{gd}^P\right), \tag{14}$$

where ϕ_u and ϕ_d are the ascending and descending mass flux, respectively. We assume negligible magma extrusion and approximately steady degassing such that $\phi_u = \phi_d$ and i_* is constant throughout the domain, yielding

$$i_* = i_a^P + i_{ga}^P - i_d^P - i_{gd}^P. \tag{15}$$

Once i_* is known, we can compute $i_a^P + i_{ga}^P$ at each pressure step using eq. 15 and $i_d^P + i_{gd}^P$. We then update i_a and i_{ga} for the entire pressure range by partitioning i_a^P and i_{ga}^P at each pressure step using MagmaSat (Gualda et al., 2012; Ghiorso & Gualda, 2015).

To compute i_*, we fix $i_a^{P_{max}} + i_{ga}^{P_{max}}$, rather than fix $i_{ga}^{P_{min}}$ as Witham (2011a) does. We can also vary $i_a^{P_{max}} + i_{ga}^{P_{max}}$ to test the effect of variable volatile content. We make this adjustment because current measurements only constrain surface gas flux (Burton et al., 2007a; Oppenheimer et al., 2009). Using surface gas flux to compute $i_{ga}^{P_{min}}$ requires the knowledge of ϕ_u, which is unavailable from data. We hence compute i_* by

$$i_* = i_a^{P_{max}} + i_{ga}^{P_{max}} - i_d^{P_{max}} - i_{gd}^{P_{max}}. \tag{16}$$

After updating i_a and i_{ga}, we iterate eqs. 12, 13, 16, and 15 until reaching a steady state.

3 Results

3.1 Actively Segregating Bubbles Can Lead to Substantial Magma Mixing in Volcanic Conduits

To understand how actively segregating bubbles create magma mixing during bidirectional conduit flow, we perform a series of simulations summarized in table 2 with selected snapshots shown in fig. 4. Together, the actively segregating and passively advecting bubbles represent total bubble fractions (ϕ+$\Delta\phi_p$) between 2.1% and 12.0% in our simulations (table 2). While higher bubble volume fractions are possible, we focus on this range to understand the onset of mixing and flow collapse. To account for the different flow speeds in our simulations, we compare them at the same nondimensional time $\hat{t}$. We use R as the characteristic length and the vertical speed at the center line of the analytical solution enforced at the bottom boundary (setting $y = 0$ in eq. 6), v_c, as the characteristic speed in our nondimensionalization (Suckale et al., 2018), thus $\hat{t} = tv_c/R$.

For constant magma properties, bubble speed depends on both bubble radius and bubble density. Using simulation No. 1 shown in fig. 4A as the baseline, we reduce bubble radius r by 30% in simulation No. 2 shown in fig. 4B and increase bubble density ρ_b to reduce the density contrast between bubble and ascending magma by 49% in simulation No. 3 shown in fig. 4C. All other parameters are constant. We select these particular values, including the unrealistically high bubble density in simulation No. 3, to keep the Stokes rise speed of an isolated bubble, $v_b = (\rho_r - \rho_b)gr^2/\mu_r$, approximately the same in simulations No. 2 and 3.

Comparing figs. 4A-C, differences in the efficiency of mixing are not immediately obvious. Quantifying the mixing factors of simulations No. 1, 2, and 3 clarifies that simulation No. 1 entails more significant mixing (Γ=0.103) than the other two cases. The wavy interface separating the two magmas entraps some of the volatile-poor magma into the volatile-rich magma. In contrast, both figs. 4B (No. 2) and C (No. 3) show a flow field with a much smaller and similar degree of mixing (Γ=0.033 and 0.039, respectively) and a stabler core-annular geometry. As compared to fig. 4A, the entrapment of volatile-poor magma into the volatile-rich magma is less frequent and entails smaller batches of magma.

Figs. 4A (No. 1) and D (No. 5) highlight the importance of both magma viscosities, μ_r and μ_p, in governing mixing. With both viscosities equally increased by 2/3, the flow field in fig. 4D becomes more stable and exhibits less mixing (Γ=0.056) than in fig. 4A. In addition to increasing both magma viscosities, we decrease bubble density in fig. 4D to ensure that the Stokes rise speed is the same in both simulations. To isolate the effect of individual magma viscosities from that of a varying viscosity contrast (Stevenson & Blake, 1998; Beckett et al., 2011; Suckale et al., 2018), we maintain a constant viscosity contrast between the magmas.

Besides phase properties (bubble speed and magma viscosities), phase proportions also affect mixing and flow stability. Figs. 4A (No. 1) and E (No. 14) highlight the importance of ϕ, the volume fraction of actively segregating bubbles. With ϕ increased to 3%, the flow field in fig. 4E becomes less stable and exhibits more mixing (Γ=0.195) than in fig. 4A. Similarly, comparing simulation No. 1 with No. 13 and simulation No. 9 with No. 15 (table 2) also demonstrates that increasing ϕ increases the degree of mixing.

Fig. 4E exhibits high mixing despite a relatively small increase in ϕ. This result suggests that mixing can be extensive even at relatively low ϕ, particularly when bubbles are segregating fast in a relatively low viscosity magma as shown by figs. 4A-D. Fig. 4F (simulation No. 6) illustrates the compound effect of increasing bubble speed and decreasing magma viscosities. In simulation No. 6, v_b is 6 times higher than in fig. 4A and the magma viscosities are a fifth of those in fig. 4A. The consequence is extensive mixing and a complete collapse of core-annular flow. The volatile-rich and volatile-poor magmas in-

Table 2. Values of variables in simulations.

Simulation No.	ρ_r(kg/m^3)	ρ_p(kg/m^3)	ρ_b(kg/m^3)	μ_r(Pa·s)	μ_p(Pa·s)	r(m)	ϕ	max($\Delta\phi_p$)	max(ΔC_{H_2O})	Sc	M	Γ	σ
1	2400	2500	600	3×10^4	9×10^4	4.3×10^{-2}	2%	5.16%	2.00%	9.94×10^5	3	0.103	0.216
2	2400	2500	600	3×10^4	9×10^4	3×10^{-2}	2%	5.16%	2.00%	2.16×10^6	3	0.033	0.034
3	2400	2500	1518	3×10^4	9×10^4	4.3×10^{-2}	2%	9.98%	2.00%	2.03×10^6	3	0.039	0.051
4	2400	2500	600	1.85×10^4	5.55×10^4	4.3×10^{-2}	2%	5.16%	2.00%	3.78×10^5	3	0.230	0.394
5	2400	2500	76.21	5×10^4	1.5×10^5	4.3×10^{-2}	2%	5.04%	2.00%	2.14×10^6	3	0.056	0.035
6	2450	2452	300	6×10^3	1.8×10^4	4.3×10^{-2}	2%	0.09%	0.04%	3.26×10^4	3	0.823	0.232
7	2400	2500	600	2×10^4	2×10^5	4.3×10^{-2}	2%	5.16%	2.00%	4.42×10^5	10	0.038	0.055
8	2400	2500	600	9×10^3	9×10^4	4.3×10^{-2}	2%	5.16%	2.00%	8.95×10^4	10	0.134	0.134
9	2400	2500	600	9×10^3	9×10^4	6×10^{-2}	2%	5.16%	2.00%	4.37×10^4	10	0.337	0.269
10	2450	2452	300	5×10^3	5×10^4	4.3×10^{-2}	2%	0.09%	0.04%	2.26×10^4	10	0.846	0.290
11	2400	2500	600	2×10^4	1×10^6	4.3×10^{-2}	2%	5.16%	2.00%	4.42×10^5	50	0.005	0.032
12	2400	2500	600	5×10^3	5×10^5	6×10^{-2}	2%	5.16%	2.00%	1.35×10^4	100	0.033	0.309
13	2400	2500	600	3×10^4	9×10^4	4.3×10^{-2}	1%	5.21%	2.00%	1.21×10^6	3	0.036	0.073
14	2400	2500	600	3×10^4	9×10^4	4.3×10^{-2}	3%	5.11%	2.00%	8.87×10^5	3	0.195	0.277
15	2400	2500	600	9×10^3	9×10^4	6×10^{-2}	1.5%	5.18%	2.00%	4.76×10^4	10	0.177	0.105
16	2400	2500	700	5×10^3	2.5×10^5	6×10^{-2}	0.5%	5.53%	2.00%	2.18×10^4	50	0.002	0.007
17	2400	2500	300	3×10^4	3×10^5	4.3×10^{-2}	1%	5.50%	2.00%	1.04×10^6	10	0.001	0.001
18	2520	2550	100	5×10^3	1×10^5	6×10^{-2}	1.3%	1.21%	0.60%	1.09×10^4	20	0.569	0.419
19	2450	2550	300	8×10^3	1.6×10^5	6×10^{-2}	1.5%	4.38%	2.00%	3.09×10^4	20	0.070	0.245
20	2400	2500	700	1.6×10^3	8×10^4	6×10^{-2}	0.5%	6.03%	2.00%	2.23×10^3	50	0.007	0.002
21	2366	2500	700	5×10^3	2.5×10^5	-†	0%	7.44%	2.68%	-†	50	0.001	0.001
22	2400	2500	100	2×10^4	1×10^5	-†	0%	4.17%	2.00%	-†	5	0.0002	0.002
Example magma properties at deep and shallow conduit:													
Deep	2400	2500	700	5×10^3	2.5×10^5	3×10^{-2}	0.5%	6.03%	2.00%	9.33×10^4	50		
Shallow	2300	2500	100	1×10^4	1.25×10^5	8×10^{-2}	3%	11.08%	4.00%	2.23×10^4	12.5		

† The values are missing because no actively segregating bubbles are present ($\phi = 0$).

terpenetrate significantly, with highly varied moving direction both horizontally and vertically.

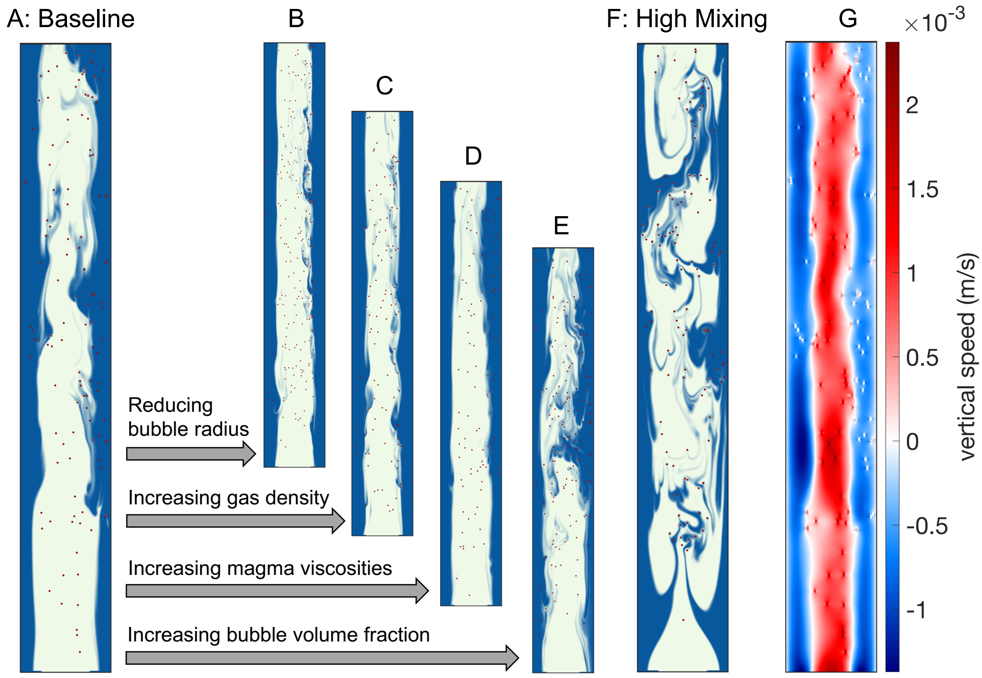

Figure 4. **(A)-(E)**: Snapshots taken at nondimensional time $\hat{t}$=40 (the characteristic time is R/v_c) from simulations No. 1 (A), No. 2 (B), No. 3 (C), No. 5 (D), and No. 14 (E). **(F)**: Snapshot taken at $\hat{t}$=6.5 from simulation No. 6, which has the highest bubble speed and the lowest magma viscosities among simulations in (A)-(F). **(G)**: Corresponding vertical speed field of (A).

Even at bubble fractions as low as 2%, bubbles with radii much smaller than the conduit width can have a profound effect on conduit flow. To understand the physical mechanism, we quantify the stress disruptions created by bubbles stirring the bidirectional interface (fig. 5). Fig. 5A shows the interfacial stress deviation, $\tau_{xy} - \tau$, where τ_{xy} is the simulated shear stress and τ is the analytical interfacial shear stress (Suckale et al., 2018). The interfacial stress deviations lead to localized interface deformation, and, if pronounced enough, to interfacial wave build-up and mixing.

We conduct a statistical analysis (fig. 5B) of the simulation results in fig. 5A. Within a period of nondimensional time $\hat{t} \in [0, 15]$, where the core-annular flow is stable, we sample points on the interface. At each point, we compute how much the stress in the vicinity of the interface deviates from the analytical solution and the distance to the nearest bubble. We exclude bubble clusters from this analysis, because the hydrodynamic stress field around a bubble cluster is dominated by the hydrodynamic interactions between bubbles, which diverge upon increasingly close contact. Fig. 5B shows that the interfacial stress deviation increases as the distance to the nearest bubble decreases, highlighting the significant stress deviation introduced at the interface by nearby bubbles.

We find that a transitional flow exists between the stable flow with relatively low mixing (e.g., figs. 4B-D) and the unstable flow with extensive mixing and complete collapse of core-annular flow(e.g., fig. 4F). For instance, simulation No. 9 shown in fig. 6A demonstrates the transitional flow, where a large batch of descending, degassed magma drips into the ascending, volatile-rich magma, disrupting the initially stable core-annular

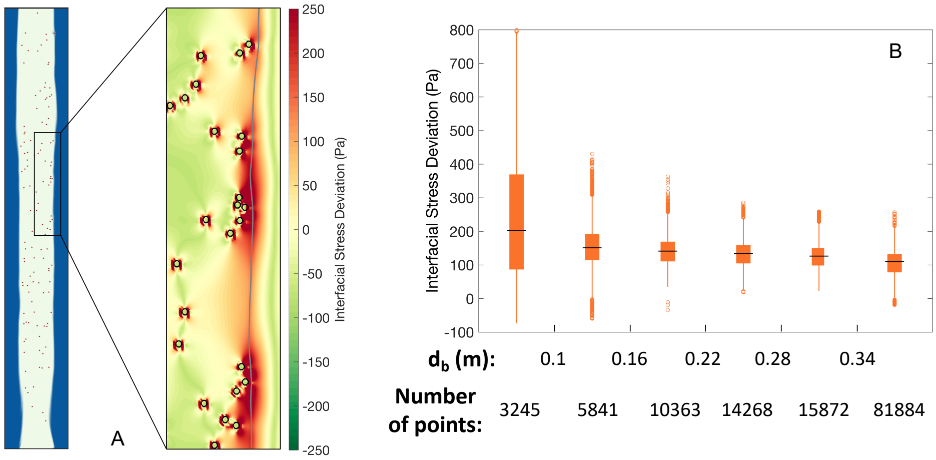

Figure 5. **(A)**: Interfacial stress deviation caused by bubbles (black circles) in the marked subregion of simulation No. 4 at $\hat{t}$=6.2. The grey curve marks the interface (c=0.5). **(B)**: Statistical analysis of the relationship between the interfacial shear stress and the vicinity of bubbles for simulation No. 4. Each sample is a point on the interface at $\hat{t} \in [0, 15]$. d_b is the distance between the sample point and its nearest bubble. The black line segments mark the median (q_2) of each group. The bottom and top of the boxes mark the 25% (q_1) and 75% (q_3) quantiles, respectively. The whiskers mark the range $[q_1 - 1.5 \times (q_3 - q_1), q_3 + 1.5 \times (q_3 - q_1)]$. The circles mark the outliers.

flow. The consequence is significant mixing, but the flow field itself recovers eventually ($\hat{t} = 40.0$ in fig. 6A). In contrast, simulation No. 10 shown in fig. 6B demonstrates the unstable flow, where pronounced interfacial waves build up at the beginning of the simulation and quickly lead to seemingly chaotic mixing. In this case, the disrupted core-annular flow never recovers.

3.2 Generalizing Simulation Results through Nondimensional Analysis

Given the low molecular diffusivity in the conduit flow model ($D = 10^{-10}\mathrm{m}^2/\mathrm{s}$), magma mixing in the absence of bubbles is negligible (e.g., simulations No. 21-22). The long-range hydrodynamic interactions of actively segregating bubbles in the volatile-rich magma lead to long-range spatial correlations that result in the diffusion of volatiles in the domain (Segre et al., 2001; Mucha et al., 2004). This mass diffusion is much more efficient than molecular diffusion, but competes with momentum diffusion in the core magma given by its viscosity. In this section, we conduct a nondimensional analysis to generalize our insights about the factors controlling mixing and flow-regime stability in bubble-bearing core-annular flow to various depths within volcanic systems.

The long-range hydrodynamic interactions of actively segregating bubbles increase the mass diffusivity. Therefore, we summarize the effects of bubble speed, magma viscosities, and bubble volume fraction as a competition between the mass diffusivity and the momentum diffusivity. High mass diffusivity facilitates the mixing of the volatile-rich and volatile-poor magmas by increasing the efficiency of mass transfer between the two magmas. In contrast, high momentum diffusivity, represented by the kinematic viscosity, leads to effective momentum transfer and suppresses the relative efficiency of mass

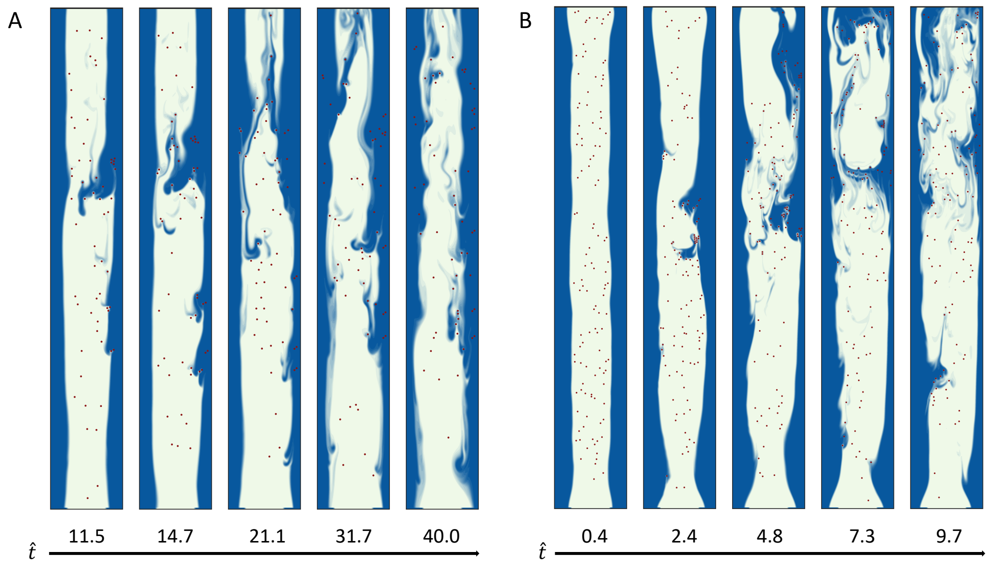

Figure 6. **(A)**: Snapshots from simulation No. 9 showing the gradual and recoverable collapse of core-annular flow (transitional flow). **(B)**: Snapshots from simulation No. 10 showing the quick and complete collapse of core-annular flow (unstable flow).

transfer. The Schmidt Number, Sc, captures this competition and is defined as

$$Sc = \frac{\mu_r}{\rho_r D_H}, \tag{17}$$

where D_H is the hydrodynamic diffusion coefficient. As the hydrodynamic interactions of actively segregating bubbles mainly exist in the volatile-rich magma, we compute Sc for the volatile-rich magma as reflected by our choice of kinematic viscosity, μ_r/ρ_r, in eq. 17. Following Segre et al. (1997, 2001), we define D_H as

$$D_H \sim \xi \Delta v, \tag{18}$$

where

$$\xi \sim r\phi^{-1/3} \tag{19}$$

is the correlation length of actively segregating bubbles, and

$$\Delta v \sim v_b \phi^{1/3} f(\phi, r, R) \tag{20}$$

is the fluctuation in bubble velocity. Here v_b is the Stokes rise speed, and

$$f(\phi, r, R) = 1 - \exp(\frac{-R}{30 r \phi^{-1/3}}). \tag{21}$$

We ignore the constants associated with eqs. 18-20 (Segre et al., 1997, 2001) because they have no effect on the relative differences in Sc for our simulations, leading to

$$Sc = \frac{\mu_r^2}{\rho_r(\rho_r - \rho_b) g r^3 f(\phi, r, R)}. \tag{22}$$

Previous laboratory studies demonstrate that increasing the viscosity contrast, M, between the volatile-rich and volatile-poor magma stabilizes the core-annular flow regime (Stevenson & Blake, 1998; Beckett et al., 2011; Suckale et al., 2018). Therefore, we run simulations with different viscosity contrasts (table 2) and use $M = \mu_p/\mu_r$ as the second nondimensional number in our analysis.

We summarize the effect of both nondimensional numbers on mixing and the stability of the core-annular flow in Fig. 7A. Decreasing Sc and M destabilizes the core-annular flow and increases the degree of magma mixing. The decrease of magma mixing and the change from more to less wavy core-annular flow from simulation No. 1 (fig. 4A) to No. 2, 3, 5 (figs. 4B-D) are associated with the increase of Sc. The increase of magma mixing from simulation No. 1 (fig. 4A) to No. 14 (fig. 4E) is consistent with the increase of Sc. Among simulations shown in fig. 4, simulation No. 6 (fig. 4F) has the smallest Sc and shows the highest degree of mixing and the most unstable flow regime. The transition value of Sc from stable to unstable flow decreases as M increases. All simulations with $M \geq 50$ show low mixing and a stable flow regime. The transition zone in fig. 7A shows the transitional flow (fig. 6A) separating the stable core-annular flow and the unstable flow (fig. 6B) that collapses quickly and irreversibly.

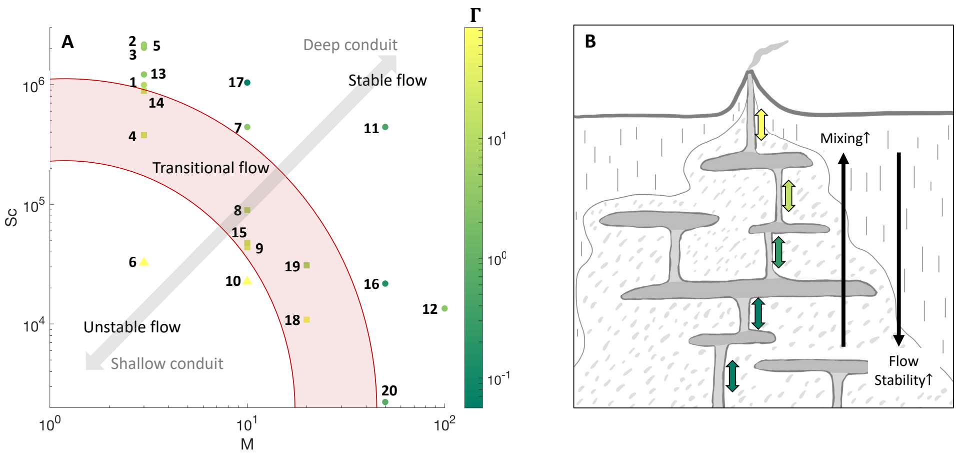

Figure 7. **(A)**: Regime diagram for the stability of core-annular flow. The numbers identify individual simulations and the color scale represents the mixing factor Γ. Round, square and triangle markers highlight stable, transitional, and unstable flow during $\hat{t} \in [0, 90]$, respectively. The inferred red transition zone (i.e. transitional flow) separates the stable and unstable flow. **(B)**: Our model indicates higher degree of mixing and less stable flow regime in the conduits towards shallower depth.

As magma ascends, the decrease in gas density due to decompression, the increase in magma viscosity due to H_2O exsolution, and the increase in bubble sizes and volume fraction result in decreasing Sc and M (example magma properties are listed in table 2). Therefore, as magma ascends, the conduit flow evolves from stable core-annular flow with relatively low mixing to unstable flow with high mixing (fig.7B). Simulations showing high mixing and unstable flow regime (simulation No. 6 and 10) are representative of shallow magma. Simulations showing low mixing and stable core-annular flow (simulation No. 16 and 20), on the other hand, are representative of deep magma. At depth with limited volatile exsolution, the majority of bubbles is advecting passively and Sc would be large. Simulations No. 21 and 22 are representative of this limit, producing a completely stable core-annular flow regime with low mixing.

3.3 Magma Mixing Alters the H_2O-CO_2 Concentration Profiles

To test the effect of different mixing factors, Γ, and different total CO_2 content at P_{max}, we compute synthetic concentration profiles and compare these to the H_2O and CO_2 concentrations in melt inclusions for Stromboli and Mount Erebus. We isolate the two processes by conducting two suites of calculations for each volcano (figs. 8A-D). In each group, we fix one process and vary the other one to test whether the two processes leave distinct observational signatures. In both cases, we fix the total amount of H_2O as the concentrations in the most volatile-rich melt inclusions, because at P_{max} H_2O is unsaturated according to MagmaSat (Gualda et al., 2012; Ghiorso & Gualda, 2015). We also fix the proportion of passively advecting bubbles in the gas phase, θ, as 0.5, and conduct a separate analysis on the effect of θ below (figs. 8E-F).

Fig. 8 compares the computed volatile concentration profiles of ascending magma to published melt-inclusion data (Métrich et al., 2010; Oppenheimer et al., 2011). We focus on the ascending magma because volatile exsolution during ascent increases crystallization, while volatile enrichment through mixing during descent (fig. 3) may facilitate resorption and thus limit the formation of melt inclusions (Witham, 2011b). Applying small degrees of mixing ($\Gamma < 0.05$) to the entire pressure range sensitively affect the relationship between CO_2 and H_2O (figs. 8A-B). Increasing mixing shifts the concentration profiles towards higher CO_2 and lower H_2O concentrations relative to the closed-system profiles ($\Gamma = 0$). However, the profiles quickly become insensitive to further mixing as shown by the profiles with $\Gamma = 0.2$ in figs. 8A-B. We do not consider $\Gamma > 0.2$ in fig. 8, because core-annular flow is no longer stable in this limit (e.g., fig. 7A).

We have included a few examples for synthetic volatile concentration profiles that are based on Γ increasing during magma ascent, because our simulations suggest that Γ is likely depth-dependent in a given volcanic systems (see fig. 7). When Γ is fixed at 1 atm, increasing the initial value of Γ at depth shifts the computed profiles notably towards higher CO_2 and lower H_2O concentrations, as shown by the blue curves in figs. 8A-B. However, the results of both constant and depth-variable mixing factors appear consistent with data (figs. 8A-B), suggesting that the data does not currently afford the resolution necessary to identify potential depth-variability in mixing.

Varying the mixing factor does not only affect the volatile concentration in melt inclusions, but also the volatile concentration in the gas flux at the surface. To illustrate this effect, we define λ as the ratio of the weight of H_2O and CO_2 in the gas phase at the surface (see legend of figs. 8A-B). Without mixing ($\Gamma = 0$), $\lambda \approx (H_2O/CO_2)_{P_{max}}$. Our simulations show that increasing magma mixing decreases the value of λ. With mixing, the observed ratio of the weight of H_2O and CO_2 in the gas phase at the surface would be lower than the ratio in the primitive magma at depth. According to the surface-gas-flux data, λ ranges from 0.82 to 2.49 and 0.56 to 0.79 at Stromboli and Mount Erebus, respectively (Burton et al., 2007a; Oppenheimer et al., 2009).

For both sample 97009 from Mount Erebus and all Stromboli samples, accounting for magma mixing results in concentration profiles that are more consistent with observations than either open- or closed-system degassing alone (figs. 8A-B). Other samples from Mount Erebus are clearly distinct from sample 97009 and approximately represent a closed-system profile (open circles and purple curve in fig. 8A). Sample 97009 is also much more H_2O-rich than the other samples from Erebus, but the whole-rock composition and occurrence of sample 97009 (tephriphonolite palagonite breccia) is non-unique among all samples (Oppenheimer et al., 2011).

We emphasize that we are unable to constrain Γ through the melt-inclusion data exactly due to data scatter and the low sensitivity of the profile to Γ at high mixing. Nonetheless, the results in figs. 8A-B indicate that high mixing throughout the system is unlikely because it results in much lower λ (H_2O/CO_2 in surface gas) than observed at Strom-

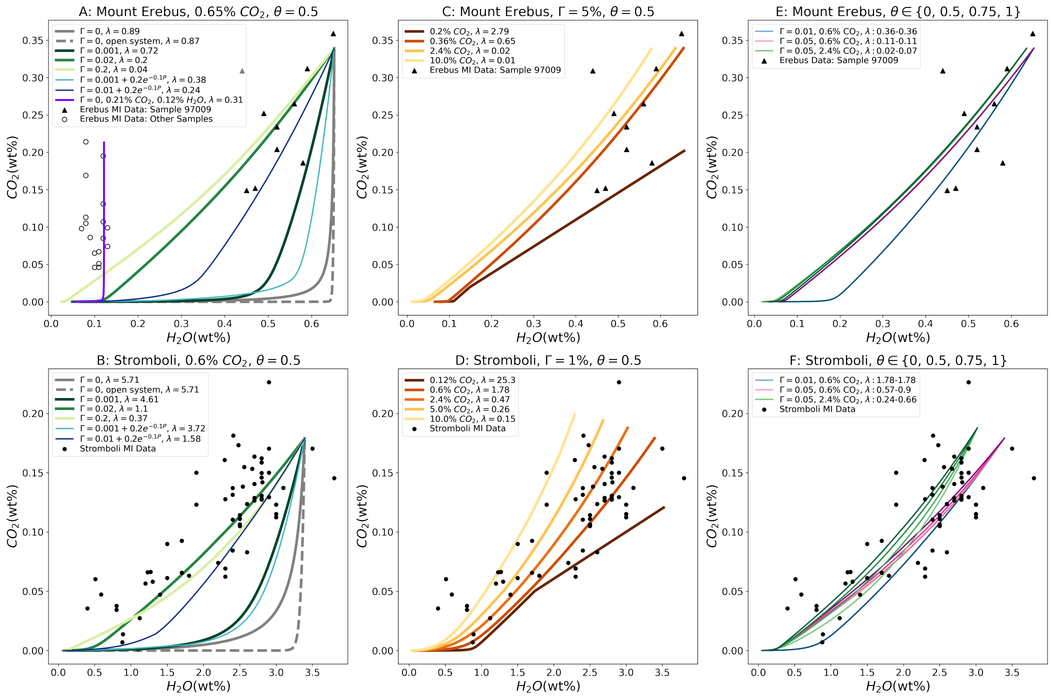

Figure 8. **(A)-(B)**: H_2O-CO_2 concentration profiles of ascending magma with varied mixing factors, constant θ, and constant total CO_2 and H_2O contents at P_{max}. The blue curves represent profiles with mixing factors varied with pressure. **(C)-(D)**: H_2O-CO_2 concentration profiles of ascending magma with varied total CO_2 content but constant H_2O content at P_{max}, constant θ, and constant mixing factors. **(E)-(F)**: Three groups of H_2O-CO_2 concentration profiles of ascending magma with different mixing factors and total CO_2 content at P_{max}. The four curves from light to dark within each group correspond to $\theta = 0, 0.5, 0.75$ and 1.

boli and Mount Erebus (Burton et al., 2007a; Oppenheimer et al., 2009). Therefore, when analyzing the effect of total CO_2 content below, we only consider low mixing ($\Gamma \leq 0.05$).

Figs. 8C-D show that for a fixed Γ, varying total CO_2 content at P_{max} also significantly alters the volatile concentration profiles and further improves the fit between model and data. Increasing CO_2 content shifts the profiles towards higher CO_2 and lower H_2O concentrations, especially at high pressures. This effect is distinct from the effect of magma mixing. Increasing CO_2 content also decreases λ, as shown in figs. 8C-D.

Figs. 8E-F show the effects of the proportion of passively advecting bubbles in the gas phase, θ, on the concentration profiles and λ. For each volcano, we conduct three groups of calculation with different Γ and CO_2 contents. For both volcanoes, increasing θ increases λ and slightly shifts the profiles towards higher CO_2 and lower H_2O concentrations, although the effect is insignificant for Mount Erebus, as shown by the indistinguishable curves in each group in fig. 8E. Increasing mixing and CO_2 contents enhances the effect of θ, especially for Stromboli (fig. 8F).

While some melt inclusions may still form in descending magma, fig. 9A shows that the trend of descending profiles is generally similar to that of the corresponding ascending profiles, but shifted to slightly lower H_2O and CO_2 concentrations. Therefore, the ascending profiles plotted in figs. 8A-F are representative of the recorded compositions. Figs. 9B and C show the CO_2 and H_2O concentrations against pressure, respectively. At high pressures, ascending and descending profiles are approximately parallel, with a distance inversely correlated Γ. At low pressures, the distance between ascending and descending profiles decreases and becomes 0 at 1 atm, where the ascending magma degases and then descends.

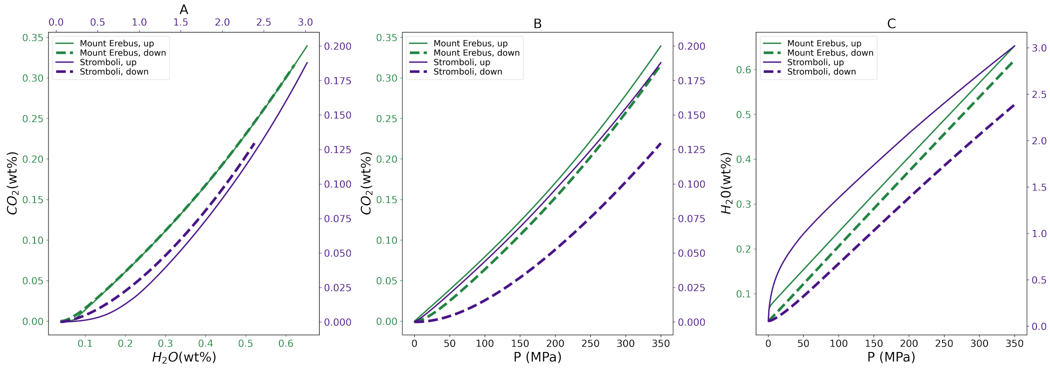

Figure 9. Comparison of computed ascending and descending profiles for Mount Erebus ($\Gamma = 0.05$, 0.6% CO_2, $\theta = 0.5$) and Stromboli ($\Gamma = 0.01$, 2.4% CO_2, $\theta = 0.5$). Solid and dashed curves correspond to ascending (up) and descending (down) profiles, respectively. **(A)**: H_2O-CO_2 concentration profiles. **(B)**: Pressure-CO_2 profiles. **(C)**: Pressure-H_2O profiles.

In the analysis above, we apply mixing factors derived for conduit segments to the entire pressure range of volcanic systems. However, plumbing systems consist of multiple different elements that can affect H_2O-CO_2 concentration profiles (see fig. 1D). Tabular lenses connect different, potentially transient vertical conduit segments and lava lakes or a largely crystalline plug near the free surface may limit the ascent of volatile-rich magma. In fig. 10 we use Stromboli as an example for a sensitivity analysis assessing the effect of P_{min} and the presence of tabular lenses on volatile-concentration profiles. In cases where the top of the bidirectional flow is at the surface, $P_{min} > 1$ atm, but at Stromboli a crystal-rich plug is thought to extend to a depth of 700-800 m (Landi et al., 2004). Fig. 10A shows that increasing P_{min} to account for this plug slightly shifts the H_2O-CO_2 concentration profile towards lower higher H_2O concentrations at low pressures. Here P_{min} =2.4 MPa and 18 MPa approximately correspond to depths of 100 m and 700 m, respectively.

In a tabular lens, the ascending magma entering from the bottom and the descending magma entering from the top may mix extensively. Since tabular lenses are likely limited in vertical extent, we assume that a lens takes up one pressure step. Therefore, at this pressure step, instead of applying eqs. 12 and 15, we enforce that the ascending and descending magma shares the same dissolved volatile content. The rule for exsolved volatile content stays unchanged because the gas phase still tend to ascend in the lenses. Figs. 10B-D show that the presence of a tabular lens at the depth of 4 km (Métrich et al., 2010) creates a kink at the corresponding location on the profiles without fundamentally changing the trend. The results are a reflection of the assumed geometry in fig. 1, where tabular lenses divide the system-scale convection into sub-convections between lenses. We emphasize that we do not attempt to fully capture the dynamic role of tabular lenses for degassing, but merely attempt to provide a sensitivity analysis of our results.

4 Discussion

Analogue laboratory models illustrate the basic physical processes that govern bidirectional flow (Stevenson & Blake, 1998; Beckett et al., 2011), but are highly idealized

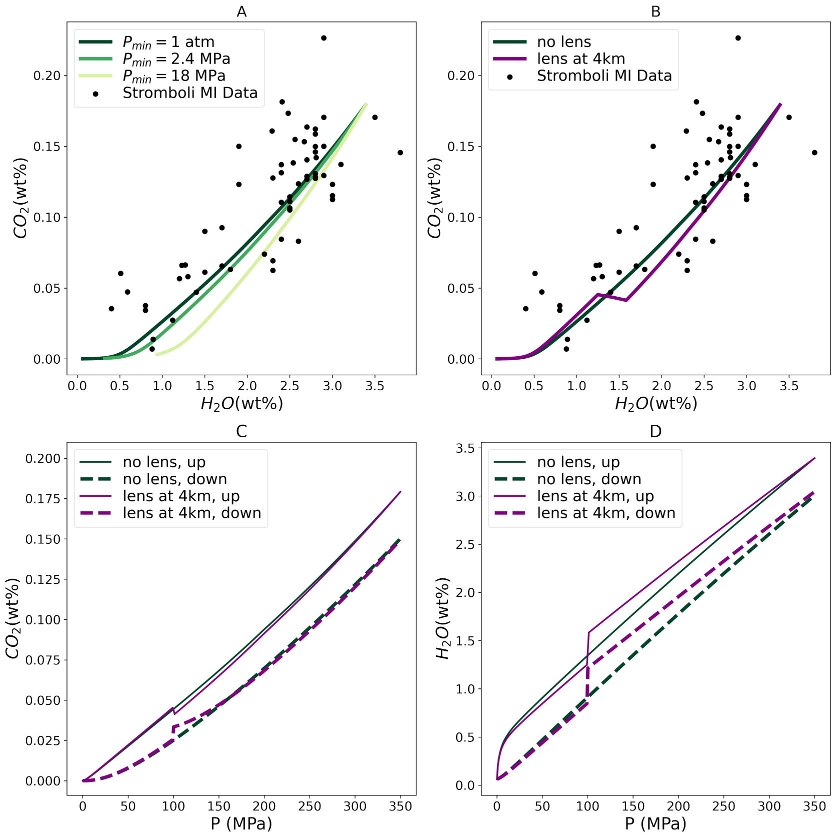

Figure 10. **(A)**: Effect of P_{min} on H_2O-CO_2 concentration profiles. **(B)**: Comparison of H_2O-CO_2 concentration profiles with and without tabular lens. **(C)**: Comparison of pressure-CO_2 profiles with and without tabular lens. **(D)**: Comparison of pressure-H_2O profiles with and without tabular lens. All the profiles are for Stromboli, with 0.6% CO_2, θ =0.5, and Γ =0.02.

representations of actual volcanic systems. Conduit models can help bridge the gap between laboratory and volcanic scales (Suckale et al., 2018; Fowler & Robinson, 2018), but are difficult to test against observational data. The challenge arises because observational data, such as melt inclusion compositions and surface gas flux (Métrich et al., 2001; Burton et al., 2007a; Oppenheimer et al., 2009, 2011; Métrich et al., 2010; Ilanko et al., 2015; Rasmussen et al., 2017), are the product of multiscale processes while most existing conduit models operate at the volcano scale and do not entail testable model predictions at the scale of individual bubbles or crystals.

This study attempts to advance our ability to gain insights into degassing-driven flow processes in volcanic conduits from melt-inclusion and surface-flux data. To do that, we integrate numerical simulations of bidirectional conduit flow at the scale of individual bubbles with a system-scale calculation of H_2O-CO_2 concentration profiles. We analyze how the presence of bubbles affects the degree of magma mixing in vertical conduit segments (fig. 4). We demonstrate that the presence of gas bubbles, even bubbles that are much smaller than the conduit radius, can trigger significant mixing and even flow-regime collapse at viscosity contrasts that would be stable in the absence of bubbles (Stevenson & Blake, 1998; Suckale et al., 2018).

Previous laboratory studies have shown that a finite viscosity contrast between ascending and descending magma is necessary for stable core-annular flow (Stevenson &

Blake, 1998; Huppert & Hallworth, 2007; Beckett et al., 2011). However, contrary to the syrups used in these experiments, magmas in volcanic systems are not pure liquids. They contain crystals and bubbles of various sizes and the presence of these additional gas and solid phases affects the stability of the flow. For instance, simulations with the same viscosity contrast ($M = 3$ for simulations No. 1-6, 13, 14, $M = 10$ for simulations No. 7-10, 15, 17, $M = 20$ for simulations No. 18-19, $M = 50$ for simulations No. 11, 16, 20) can show significant differences in mixing and stability when they differ in the Schmidt number of the volatile-rich magma (fig. 7). The Schmidt number represents the non-dimensional ratio of momentum diffusivity to bubble mass diffusivity in the volatile-rich magma, implying that flows with low Schmidt number are particularly prone to mixing and instability.

Our simulations show that bubbles locally increase the interfacial stress (fig. 5). This interfacial stress deviation disrupts the linearly unstable (Selvam et al., 2007, 2009; Martin et al., 2009) but nonlinearly stable interface (Hickox, 1971; Ullmann & Brauner, 2004; Suckale et al., 2018). In the absence of bubbles, linear growth of instability is suppressed by the nonlinear interaction between the growing interface wave and viscous damping in the two magmas (Hickox, 1971; Ullmann & Brauner, 2004; Suckale et al., 2018). The presence of bubbles introduces additional perturbations into this metastable flow configuration (e.g., fig. 4B) that can trigger wave breaking (e.g., fig. 4A) and mixing (e.g., fig. 4F).

The finding that bubbles with radii much smaller than the conduit width can have such a significant effect may appear surprising. However, flow-regime stability at the conduit scale ultimately hinges on interface stability, which in turn hinges on the disruptions introduced by the bubbles. The relevant scale comparison is thus not between the bubble radius and the conduit width, but between the bubble radius and the width of the interface separating volatile-rich and volatile-poor magma. So long as a well-defined interface exists, these scales are comparable. Similarly to prior experimental studies focused on understanding bidirectional flow in volcanic systems (Stevenson & Blake, 1998; Huppert & Hallworth, 2007; Beckett et al., 2011), we only focus on magmas with low diffusivities in our simulations.

Our simulations suggest that some degree of mixing is almost inevitable in core-annular flow unless bubbles remain very small until close to the upper surface. This scenario could occur particularly for very low volatile contents and relatively high magma viscosity. Magma mixing tends to increase at shallow depth, potentially to the point of triggering core-annular flow collapse (fig. 7). The reason is that the gas phase plays an increasingly important role in the system dynamics at decreasing depth below the surface, because of continued exsolution, bubble growth, and gas decompression (e.g., H. Gonnermann & Manga, 2013).

If magma mixing is as common as our simulations suggest, it would be reflected in observational data. To test the compatibility of our model results with observations, we compute the H_2O-CO_2 concentration profiles associated with different mixing factors building on Witham (2011a). The fit between modeled and measured volatile concentrations increases notably when accounting for magma mixing, even for low mixing factors (figs. 8A-B). However, given the significant scatter in the melt-inclusion data, there is a relatively wide range of mixing factors that would be compatible with the data including depth-variable mixing factors.

Figs. 8C-D show that varying CO_2 content also improves the match between modeled and measured volatile concentrations, as also argued by previous studies (e.g., Burton et al., 2007b; Métrich et al., 2010; Rasmussen et al., 2017). Both Burton et al. (2007b) and Métrich et al. (2010) estimate that the amount of CO_2 content at Stromboli is 2.4%. In our simulations, this CO_2 content results in λ=0.47 (H_2O/CO_2 in the gas phase at the surface) as shown in fig. 8D. Even with a low degree of mixing, this resultant λ is outside the range 0.82-2.49 observed at Stromboli (Burton et al., 2007a). Increased mixing further decreases λ due to more loss of H_2O to the descending magma.

CO_2 fluxing might also alter the volatile-concentration profile at depth, as discussed by Edmonds (2008), but it may require tens of weight percent of CO_2 to match melt-inclusion and surface-gas-flux data by invoking CO_2 fluxing. Magma with such a high gas content would start approaching a foamy structure and would be prone to fragmentation at low pressure (H. M. Gonnermann, 2015). We hence consider it unlikely that magma flow during relatively quiescent, passive degassing phases exhibits such a high gas content. Our results suggest that when accounting for magma mixing, it is unnecessary to invoke a possibly unrealistic large amount of CO_2 for reproducing melt-inclusion data. Fig. 8D shows that a CO_2 content of 0.6% results in λ=1.78, which is in the observed range (Burton et al., 2007a).

At Erebus, sample 97009 clearly stands out from the rest (see figs. 8) in being much more H_2O-rich. Oppenheimer et al. (2011) proposed that Mount Erebus is occasionally fed by volatile-rich magma but continuously flushed by CO_2-rich fluid. The resultant dry magma leads to high magma viscosity and thus low mixing. This idea is compatible with our model results: The purple curve in figs. 8A and C shows that the closed-system profile matches the data. Assuming complete degassing of CO_2 and H_2O, the calculated λ is consistent with the surface-gas-flux measurements. Sample 97009 may have formed shortly after the injection of volatile-rich magma, which decreases magma viscosity and increases mixing.

The results of the volatile-concentration model show that variable magma mixing and CO_2 fluxing contribute to the pronounced scatter in melt-inclusion data (fig. 8). These two factors, however, are only associated with the average magma composition. Another likely cause of the scatter demonstrated by our conduit-flow model is the large heterogeneity in local magma compositions. While substantial mixing of the volatile-rich and volatile-poor magma can happen, our simulations show that the resultant mixtures are highly heterogeneous (figs. 4 and 6) because of the low diffusivity. This behavior indicates that the composition of local magma entrapped by melt inclusions may differ significantly from the average, resulting in scatter in melt-inclusion data.

We emphasize that several other processes not considered in our study contribute to the pronounced scatter in melt-inclusion data. They include uncertainties in measurements (Métrich & Wallace, 2008; Métrich et al., 2010; Oppenheimer et al., 2011), disequilibrium degassing potentially generating CO_2-oversaturated melt (Pichavant et al., 2013) and crystallization affecting volatile solubility (Gualda et al., 2012; Ghiorso & Gualda, 2015). In addition, the complex geometry of some volcanic plumbing systems may introduce variability. At shallow depth, some conduits flare out into lava lakes such as at Mount Erebus, altering both mixing and surface gas flux (Oppenheimer et al., 2009). At deep depth, volcanic conduits are thought to be connected to heterogeneous and largely crystalline transcrustal plumbing systems (Cashman et al., 2017; Magee et al., 2018). Melt inclusions that form at considerable depth (Métrich et al., 2001, 2010; Oppenheimer et al., 2011; Rasmussen et al., 2017) might hence sample a different portion of the plumbing system and record processes not considered here.

Despite these caveats, our analysis suggests that melt inclusions might offer the opportunity to constrain magma mixing in volcanic conduits and variations in CO_2 fluxing over time. Both of these processes contribute to variability in the surface gas flux, which is correlated with the eruptive cycles of persistently degassing volcanoes (Burton et al., 2007a; Oppenheimer et al., 2009; Ilanko et al., 2015). Constraining their inherent variability over multiple eruptive cycles hence has the potential for increasing the constraints we can bring to bear in conduit-flow models. We hence suggest that with improved measurement accuracy and reduced uncertainty, disaggregating the scattered melt-inclusion data could help us track and better understand the evolving flow conditions in volcanic conduits, as already attempted in Spilliaert et al. (2006) and Sides et al. (2014).

5 Conclusions

Observables such as melt inclusions provide important testimony on degassing processes at persistently active volcanoes, but these data is rarely straight-forward to interpret. Models of conduit flow, on the other hand, account for important physical processes, but are often difficult to connect to and evaluate against observational data. This study contributes towards forging a closer link between a physical conduit model for non-eruptive conditions and the volatile concentration observed in melt-inclusion data. We find that actively segregating bubbles can create significant mixing between volatile-rich and volatile-poor magma, potentially up to the point of flow collapse. This finding suggests that magma mixing is common in the conduits of persistently degassing volcanoes, but variations in CO_2 fluxing may occur simultaneously. Being able to identify the relative importance of these two processes in observational data is valuable to track and better understand the evolving flow conditions in volcanic systems. Our study shows that while both magma mixing and increasing CO_2 fluxing shifts the profiles towards higher CO_2 and lower H_2O concentrations, the observational signature of increasing CO_2 fluxing is distinct from that of magma mixing by being most prominent at high pressures. Disaggregating scattered melt-inclusion data for different volcanic centers or eruptive episodes may hence help to identify variability in degassing.

Acknowledgments

This work is supported by NSF grant 1744758 awarded to JS and by the Stanford Graduate Fellowship in Science and Engineering awarded to ZW. We thank Sandro Aiuppa, Alvaro Aravena, and other anonymous reviewers for providing thoughtful suggestions for improving this manuscript. We thank Ayla Pamukcu for providing feedback to improve the text, and Mark Ghiorso for providing support on using the ENKI server.

Open Research

v1.1.1 of the code used for the conduit-flow model and the volatile-concentration model is preserved at `https://doi.org/10.5281/zenodo.5637406` with open access. The usage instructions are provided in the README file of the repository.

Author contributions

Z.W. performed the numerical simulations, computed the concentration profiles, produced the figures and wrote most of the text. Z.Q. developed the numerical technique. J.S. conceptualized the study, advised Z.W. and contributed to the text.

References

Allard, P., Carbonnelle, J., Métrich, N., Loyer, H., & Zettwoog, P. (1994). Sulfur output and magma degassing budget of Stromboli Volcano. *Nature*, *368*, 326-330. doi: 10.1038/368326a0

Aster, E. M., Wallace, P. J., Moore, L. R., Watkins, J., Gazel, E., & Bodnar, R. J. (2016). Reconstructing CO_2 concentrations in basaltic melt inclusions using raman analysis of vapor bubbles. *Journal of Volcanology and Geothermal Research*, *323*, 148 - 162. Retrieved from `http://www.sciencedirect.com/science/article/pii/S0377027316300701` doi: https://doi.org/10.1016/j.jvolgeores.2016.04.028

Bai, L., Baker, D. R., & Rivers, M. (2008). Experimental study of bubble growth in Stromboli basalt melts at 1 atm. *Earth and Planetary Science Letters*, *267*(3-4), 533–547.

Barth, A., Newcombe, M., Plank, T., Gonnermann, H., Hajimirza, S., Soto, G. J., et al. (2019). Magma decompression rate correlates with explosivity at basaltic volcanoes — constraints from water diffusion in olivine. *Journal of Volcanology and Geothermal Research*, *387*, 106664. Retrieved from http://www.sciencedirect.com/science/article/pii/S0377027319301192 doi: https://doi.org/10.1016/j.jvolgeores.2019.106664

Beckett, F. M., Mader, H. M., Phillips, J. C., Rust, A. C., & Witham, F. (2011). An experimental study of low-Reynolds-number exchange flow of two Newtonian fluids in a vertical pipe. *Journal of Fluid Mechanics*, *682*, 652–670. doi: 10.1017/jfm.2011.264

Bertagnini, A., Métrich, N., Landi, P., & Rosi, M. (2003). Stromboli Volcano (Aeolian Archipelago, Italy): An open window on the deep-feeding system of a steady state basaltic volcano. *Journal of Geophysical Research: Solid Earth*, *108*(B7), 2336. Retrieved from https://agupubs.onlinelibrary.wiley.com/doi/abs/10.1029/2002JB002146 doi: 10.1029/2002JB002146

Blake, S., & Campbell, I. H. (1986). The dynamics of magma-mixing during flow in volcanic conduits. *Contributions to Mineralogy and Petrology*, *94*(1), 72-81. Retrieved from https://doi.org/10.1007/BF00371228 doi: 10.1007/BF00371228

Blundy, J., Cashman, K. V., Rust, A., & Witham, F. (2010). A case for CO_2-rich arc magmas. *Earth and Planetary Science Letters*, *290*(3), 289 - 301. Retrieved from http://www.sciencedirect.com/science/article/pii/S0012821X09007365 doi: https://doi.org/10.1016/j.epsl.2009.12.013

Bowen, R. M. (1976). Theory of mixtures. In *Part i: Continuum physics* (pp. 1–127). Academic Press, New York, USA.

Bucholz, C. E., Gaetani, G. A., Behn, M. D., & Shimizu, N. (2013). Post-entrapment modification of volatiles and oxygen fugacity in olivine-hosted melt inclusions. *Earth and Planetary Science Letters*, *374*, 145 - 155. Retrieved from http://www.sciencedirect.com/science/article/pii/S0012821X13002781 doi: https://doi.org/10.1016/j.epsl.2013.05.033

Burton, M., Allard, P., Muré, F., & La Spina, A. (2007a). Magmatic gas composition reveals the source depth of slug-driven strombolian explosive activity. *Science*, *317*(5835), 227–230.

Burton, M., Mader, H., & Polacci, M. (2007b). The role of gas percolation in quiescent degassing of persistently active basaltic volcanoes. *Earth and Planetary Science Letters*, *264*(1), 46 - 60. Retrieved from http://www.sciencedirect.com/science/article/pii/S0012821X07005493 doi: https://doi.org/10.1016/j.epsl.2007.08.028

Cashman, K. V., Sparks, R. S. J., & Blundy, J. D. (2017). Vertically extensive and unstable magmatic systems: A unified view of igneous processes. *Science*, *355*(6331), eaag3055. Retrieved from https://science.sciencemag.org/content/355/6331/eaag3055 doi: 10.1126/science.aag3055

Del Bello, E., Llewellin, E. W., Taddeucci, J., Scarlato, P., & Lane, S. J. (2012). An analytical model for gas overpressure in slug-driven explosions: Insights into Strombolian volcanic eruptions. *Journal of Geophysical Research: Solid Earth*, *117*(B2), 206. Retrieved from https://agupubs.onlinelibrary.wiley.com/doi/abs/10.1029/2011JB008747 doi: https://doi.org/10.1029/2011JB008747

DiBenedetto, M., Qin, Z., & Suckale, J. (2020). Crystal aggregates record the pre-eruptive flow field in the volcanic conduit at Kilauea, Hawaii. *Science Advances*, *6*(49), eabd4850. Retrieved from https://advances.sciencemag.org/content/6/49/eabd4850 doi: 10.1126/sciadv.abd4850

Dixon, J. E., Clague, D. A., & Stolper, E. M. (1991). Degassing history of water, sulfur, and carbon in submarine lavas from Kilauea Volcano, Hawaii. *The Journal of Geology*, *99*(3), 371–394.

Eaton, J. P., Richter, D. H., & Krivoy, H. L. (1987). Cycling of magma between the summit reservoir and Kilauea Iki lava lake during the 1959 eruption of Kilauea Volcano. *US Geol. Surv. Prof. Pap*, *1350*, 1307–1335.

Edmonds, M. (2008). New geochemical insights into volcanic degassing. *Philosophical Transactions of the Royal Society A: Mathematical, Physical and Engineering Sciences*, *366*(1885), 4559–4579.

Fowler, A., & Robinson, M. (2018). Counter-current convection in a volcanic conduit. *Journal of Volcanology and Geothermal Research*, *356*, 141 - 162. Retrieved from `http://www.sciencedirect.com/science/article/pii/S0377027317304274` doi: https://doi.org/10.1016/j.jvolgeores.2018.03.004

Francis, P., Oppenheimer, C., & Stevenson, D. (1993). Endogenous growth of persistently active volcanoes. *Nature*, *366*, 554-557. doi: 10.1038/366554a0

Ghiorso, M. S., & Gualda, G. A. R. (2015). An H_2O-CO_2 mixed fluid saturation model compatible with rhyolite-MELTS. *Contributions to Mineralogy and Petrology*, *169*(6), 53. Retrieved from `https://doi.org/10.1007/s00410-015-1141-8` doi: 10.1007/s00410-015-1141-8

Giordano, D., Russell, J. K., & Dingwell, D. B. (2008). Viscosity of magmatic liquids: A model. *Earth and Planetary Science Letters*, *271*(1), 123 - 134. Retrieved from `http://www.sciencedirect.com/science/article/pii/S0012821X08002240` doi: https://doi.org/10.1016/j.epsl.2008.03.038

Gonnermann, H., & Manga, M. (2013). Dynamics of magma ascent in the volcanic conduit. In *Modeling volcanic processes: The physics and mathematics of volcanism* (pp. 55–84). Cambridge University Press.

Gonnermann, H. M. (2015). Magma fragmentation. *Annual Review of Earth and Planetary Sciences*, *43*, 431–458.

Gualda, G. A. R., Ghiorso, M. S., Lemons, R. V., & Carley, T. L. (2012). Rhyolite-MELTS: a modified calibration of MELTS optimized for silica-rich, fluid-bearing magmatic systems. *Journal of Petrology*, *53*(5), 875-890. Retrieved from `http://dx.doi.org/10.1093/petrology/egr080` doi: 10.1093/petrology/egr080

Hickox, C. E. (1971). Instability due to viscosity and density stratification in axisymmetric pipe flow. *The physics of Fluids*, *14*(2), 251–262.

Huppert, H. E., & Hallworth, M. A. (2007). Bi-directional flows in constrained systems. *Journal of Fluid Mechanics*, *578*, 95–112. doi: 10.1017/S0022112007004661

Ilanko, T., Oppenheimer, C., Burgisser, A., & Kyle, P. (2015). Transient degassing events at the lava lake of Erebus Volcano, Antarctica: Chemistry and mechanisms. *GeoResJ*, *7*, 43 - 58. Retrieved from `http://www.sciencedirect.com/science/article/pii/S2214242815000327` doi: https://doi.org/10.1016/j.grj.2015.05.001

Jaupart, C., & Vergniolle, S. (1988). Laboratory models of Hawaiian and Strombolian eruptions. *Nature*, *331*(6151), 58-60. Retrieved from `https://doi.org/10.1038/331058a0` doi: 10.1038/331058a0

Kazahaya, K., Shinohara, H., & Saito, G. (1994). Excessive degassing of Izu-Oshima Volcano: magma convection in a conduit. *Bulletin of Volcanology*, *56*(3), 207–216. Retrieved from `https://doi.org/10.1007/BF00279605` doi: 10.1007/BF00279605

Kyle, P. R. (1977). Mineralogy and glass chemistry of recent volcanic ejecta from Mt Erebus, Ross Island, Antarctica. *New Zealand Journal of Geology and Geophysics*, *20*(6), 1123-1146. Retrieved from `https://doi.org/10.1080/00288306.1977.10420699` doi: 10.1080/00288306.1977.10420699

Landi, P., Métrich, N., Bertagnini, A., & Rosi, M. (2004). Dynamics of magma mixing and degassing recorded in plagioclase at Stromboli (Aeolian Archipelago, Italy). *Contributions to Mineralogy and Petrology*, *147*(2), 213–227.

Lautze, N. C., & Houghton, B. F. (2005). Physical mingling of magma and complex eruption dynamics in the shallow conduit at Stromboli Volcano, Italy. *Geology*, *33*(5), 425–428.

Lautze, N. C., & Houghton, B. F. (2007). Linking variable explosion style and magma textures during 2002 at Stromboli Volcano, Italy. *Bulletin of Volcanology*, *69*(4), 445-460. Retrieved from `https://doi.org/10.1007/s00445-006-0086-1` doi: 10.1007/s00445-006-0086-1

Lesher, C. E., & Spera, F. J. (2015). Thermodynamic and transport properties of silicate melts and magma. In *The encyclopedia of volcanoes* (pp. 113–141). Elsevier.

Levine, A., Ramaswamy, S., Frey, E., & Bruinsma, R. (1998). Screened and unscreened phases in sedimenting suspensions. *Physical review letters*, *81*(26), 5944.

Liu, Y., Anderson, A., Wilson, C., Davis, A., & Steele, I. (2006). Mixing and differentiation in the Oruanui rhyolitic magma, Taupo, New Zealand: Evidence from volatiles and trace elements in melt inclusions. *Contributions to Mineralogy and Petrology*, *151*, 71-87. doi: 10.1007/s00410-005-0046-3

Magee, C., Stevenson, C. T. E., Ebmeier, S. K., Keir, D., Hammond, J. O. S., Gottsmann, J. H., et al. (2018). Magma plumbing systems: A geophysical perspective. *Journal of Petrology*, *59*(6), 1217-1251. Retrieved from `https://doi.org/10.1093/petrology/egy064` doi: 10.1093/petrology/egy064

Martin, J., Rakotomalala, N., Salin, D., & Talon, L. (2009). Convective/absolute instability in miscible core-annular flow. part 1: Experiments. *Journal of fluid mechanics*, *618*, 305.

Métrich, N., Allard, P., Bertagnini, A., & Di Muro, A. (2011). Comment on 'conduit convection, magma mixing, and melt inclusion trends at persistent degassing volcanoes' by Fred Witham, published in Earth Planetary Science Letters (2011) 301, 345-352. *Earth and Planetary Science Letters*, *306*(3-4), 306–308.

Métrich, N., Bertagnini, A., Landi, P., & Rosi, M. (2001). Crystallization driven by decompression and water loss at Stromboli Volcano (Aeolian Islands, Italy). *Journal of Petrology*, *42*(8), 1471-1490. Retrieved from `http://dx.doi.org/10.1093/petrology/42.8.1471` doi: 10.1093/petrology/42.8.1471

Métrich, N., Bertagnini, A., & Muro, A. (2010). Conditions of magma storage, degassing and ascent at Stromboli: New insights into the volcano plumbing system with inferences on the eruptive dynamics. *Journal of Petrology*, *51*, 603-626. doi: 10.1093/petrology/egp083

Métrich, N., & Wallace, P. J. (2008). Volatile abundances in basaltic magmas and their degassing paths tracked by melt inclusions. *Reviews in Mineralogy and Geochemistry*, *69*, 363 - 402. doi: https://doi.org/10.2138/rmg.2008.69.10

Molina, I., Burgisser, A., & Oppenheimer, C. (2012). Numerical simulations of convection in crystal-bearing magmas: A case study of the magmatic system at Erebus, Antarctica. *Journal of Geophysical Research: Solid Earth*, *117*(B7), 209. Retrieved from `https://agupubs.onlinelibrary.wiley.com/doi/abs/10.1029/2011JB008760` doi: 10.1029/2011JB008760

Moussallam, Y., Bani, P., Curtis, A., Barnie, T., Moussallam, M., Peters, N., et al. (2016). Sustaining persistent lava lakes: Observations from high-resolution gas measurements at Villarrica Volcano, Chile. *Earth and Planetary Science Letters*, *454*, 237 - 247. Retrieved from `http://www.sciencedirect.com/science/article/pii/S0012821X16304927` doi: https://doi.org/10.1016/j.epsl.2016.09.012

Moussallam, Y., Oppenheimer, C., Scaillet, B., Buisman, I., Kimball, C., Dunbar, N., et al. (2015). Megacrystals track magma convection between reservoir and surface. *Earth and Planetary Science Letters*, *413*, 1–12.

Mucha, P. J., Tee, S.-Y., Weitz, D. A., Shraiman, B. I., & Brenner, M. P. (2004). A model for velocity fluctuations in sedimentation. *Journal of fluid mechanics*, *501*, 71–104.

Oppenheimer, C., Lomakina, A. S., Kyle, P. R., Kingsbury, N. G., & Boichu,

M. (2009). Pulsatory magma supply to a phonolite lava lake. *Earth and Planetary Science Letters*, *284*(3), 392 - 398. Retrieved from http://www.sciencedirect.com/science/article/pii/S0012821X09002805 doi: https://doi.org/10.1016/j.epsl.2009.04.043

Oppenheimer, C., Moretti, R., Kyle, P. R., Eschenbacher, A., Lowenstern, J. B., Hervig, R. L., & Dunbar, N. W. (2011). Mantle to surface degassing of alkalic magmas at Erebus Volcano, Antarctica. *Earth and Planetary Science Letters*, *306*(3), 261 - 271. Retrieved from http://www.sciencedirect.com/science/article/pii/S0012821X11002111 doi: https://doi.org/10.1016/j.epsl.2011.04.005

Palma, J. L., Calder, E. S., Basualto, D., Blake, S., & Rothery, D. A. (2008). Correlations between SO_2 flux, seismicity, and outgassing activity at the open vent of Villarrica Volcano, Chile. *Journal of Geophysical Research: Solid Earth*, *113*(B10), 201.

Pichavant, M., Di Carlo, I., Rotolo, S. G., Scaillet, B., Burgisser, A., Le Gall, N., & Martel, C. (2013). Generation of CO_2-rich melts during basalt magma ascent and degassing. *Contributions to Mineralogy and Petrology*, *166*(2), 545-561. Retrieved from https://doi.org/10.1007/s00410-013-0890-5 doi: 10.1007/s00410-013-0890-5

Qin, Z., Allison, K., & Suckale, J. (2020). Direct numerical simulations of viscous suspensions with variably shaped crystals. *Journal of Computational Physics*, *401*, 109021. Retrieved from https://www.sciencedirect.com/science/article/pii/S0021999119307272 doi: https://doi.org/10.1016/j.jcp.2019.109021

Qin, Z., Soldati, A., Velazquez Santana, L. C., Rust, A. C., Suckale, J., & Cashman, K. V. (2018). Slug stability in flaring geometries and ramifications for lava lake degassing. *Journal of Geophysical Research: Solid Earth*, *123*(12), 10,431-10,448. Retrieved from https://agupubs.onlinelibrary.wiley.com/doi/abs/10.1029/2018JB016113 doi: 10.1029/2018JB016113

Qin, Z., & Suckale, J. (2017). Direct numerical simulations of gas–solid–liquid interactions in dilute fluids. *International Journal of Multiphase Flow*, *96*, 34 - 47. doi: https://doi.org/10.1016/j.ijmultiphaseflow.2017.07.008

Qin, Z., & Suckale, J. (2020). Flow-to-sliding transition in crystal-bearing magma. *Journal of Geophysical Research: Solid Earth*, *125*(2), e2019JB018549.

Rasmussen, D. J., Kyle, P. R., Wallace, P. J., Sims, K. W. W., Gaetani, G. A., & Phillips, E. H. (2017). Understanding degassing and transport of CO_2-rich Alkalic magmas at Ross Island, Antarctica using olivine-hosted melt inclusions. *Journal of Petrology*, *58*(5), 841-861. Retrieved from https://dx.doi.org/10.1093/petrology/egx036 doi: 10.1093/petrology/egx036

Ruth, D. C. S., Costa, F., Bouvet de Maisonneuve, C., Franco, L., Cortés, J. A., & Calder, E. S. (2018). Crystal and melt inclusion timescales reveal the evolution of magma migration before eruption. *Nature Communications*, *9*(1), 2657. doi: 10.1038/s41467-018-05086-8

Schmitt, A. K. (2001). Gas-saturated crystallization and degassing in large-volume, crystal-rich dacitic magmas from the Altiplano-Puna, northern Chile. *Journal of Geophysical Research: Solid Earth*, *106*(B12), 30561-30578. Retrieved from https://agupubs.onlinelibrary.wiley.com/doi/abs/10.1029/2000JB000089 doi: 10.1029/2000JB000089

Segre, P. N., Herbolzheimer, E., & Chaikin, P. (1997). Long-range correlations in sedimentation. *Physical Review Letters*, *79*(13), 2574.

Segre, P. N., Liu, F., Umbanhowar, P., & Weitz, D. A. (2001). An effective gravitational temperature for sedimentation. *Nature*, *409*(6820), 594–597.

Selvam, B., Merk, S., Govindarajan, R., & Meiburg, E. (2007). Stability of miscible core–annular flows with viscosity stratification. *Journal of Fluid Mechanics*, *592*, 23–49.

Selvam, B., Talon, L., Lesshafft, L., & Meiburg, E. (2009). Convective/absolute instability in miscible core-annular flow. part 2. numerical simulations and nonlinear global modes. *Journal of fluid mechanics*, *618*, 323.

Shinohara, H. (2008). Excess degassing from volcanoes and its role on eruptive and intrusive activity. *Reviews of Geophysics*, *46*(4), 5. Retrieved from `https://agupubs.onlinelibrary.wiley.com/doi/abs/10.1029/2007RG000244` doi: https://doi.org/10.1029/2007RG000244

Sides, I., Edmonds, M., Maclennan, J., Houghton, B., Swanson, D., & Steele-MacInnis, M. (2014). Magma mixing and high fountaining during the 1959 Kīlauea Iki eruption, Hawai'i. *Earth and Planetary Science Letters*, *400*, 102 - 112. Retrieved from `http://www.sciencedirect.com/science/article/pii/S0012821X14003264` doi: https://doi.org/10.1016/j.epsl.2014.05.024

Spilliaert, N., Métrich, N., & Allard, P. (2006). S-Cl-F degassing pattern of water-rich alkali basalt: modelling and relationship with eruption styles on Mount Etna Volcano. *Earth and Planetary Science Letters*, *248*(3-4), 772–786.

Stevenson, D. S., & Blake, S. (1998). Modelling the dynamics and thermodynamics of volcanic degassing. *Bulletin of Volcanology*, *60*(4), 307–317. Retrieved from `https://doi.org/10.1007/s004450050234` doi: 10.1007/s004450050234

Stoiber, R., & Williams, S. (1986). Sulfur and halogen gases at Masaya caldera complex, Nicaragua: total flux and variations with time. *Journal of Geophysical Research*, *91*, 12,215-12,231.

Suckale, J., Qin, Z., Picchi, D., Keller, T., & Battiato, I. (2018). Bistability of buoyancy-driven exchange flows in vertical tubes. *Journal of Fluid Mechanics*, *850*, 525–550. doi: 10.1017/jfm.2018.382

Sweeney, D., Kyle, P. R., & Oppenheimer, C. (2008). Sulfur dioxide emissions and degassing behavior of Erebus Volcano, Antarctica. *Journal of Volcanology and Geothermal Research*, *177*(3), 725 - 733. Retrieved from `http://www.sciencedirect.com/science/article/pii/S0377027308000553` doi: https://doi.org/10.1016/j.jvolgeores.2008.01.024

Tong, P., & Ackerson, B. J. (1998). Analogies between colloidal sedimentation and turbulent convection at high Prandtl numbers. *Physical Review E*, *58*(6), R6931.

Toramaru, A. (2014). On the second nucleation of bubbles in magmas under sudden decompression. *Earth and Planetary Science Letters*, *404*, 190–199.

Tryggvason, G., Dabiri, S., Aboulhasanzadeh, B., & Lu, J. (2013). Multiscale considerations in direct numerical simulations of multiphase flows. *Physics of Fluids*, *25*(3), 031302. Retrieved from `https://doi.org/10.1063/1.4793543` doi: 10.1063/1.4793543

Ullmann, A., & Brauner, N. (2004). Closure relations for the shear stress in two-fluid models for core-annular flow. *Multiphase Science and Technology*, *16*(4), 355-387.

Wadsworth, F. B., Kennedy, B. M., Branney, M. J., von Aulock, F. W., Lavallée, Y., & Menendez, A. (2015). Exhumed conduit records magma ascent and drain-back during a Strombolian eruption at Tongariro Volcano, New Zealand. *Bulletin of Volcanology*, *77*(9), 1–10.

Wallace, P. J. (2005). Volatiles in subduction zone magmas: concentrations and fluxes based on melt inclusion and volcanic gas data. *Journal of Volcanology and Geothermal Research*, *140*(1), 217 - 240. Retrieved from `http://www.sciencedirect.com/science/article/pii/S0377027304002884` doi: https://doi.org/10.1016/j.jvolgeores.2004.07.023

Wei, Z., Qin, Z., & Suckale, J. (2021). *Code repo for "Magma mixing during conduit flow is reflected in melt-inclusion data from persistently degassing volcanoes".* Zenodo. Retrieved from `https://doi.org/10.5281/zenodo.5637406` doi: 10.5281/zenodo.5637406

Witham, F. (2011a). Conduit convection, magma mixing, and melt inclusion trends at persistently degassing volcanoes. *Earth and Planetary Science Letters*, *301*(1), 345 - 352. Retrieved from http://www.sciencedirect.com/science/article/pii/S0012821X10007120 doi: https://doi.org/10.1016/j.epsl.2010.11.017

Witham, F. (2011b). Conduit convection, magma mixing, and melt inclusion trends at persistently degassing volcanoes: Reply to comment by Métrich et al. (2011). *Earth and Planetary Science Letters*, *306*(3), 309 - 311. Retrieved from http://www.sciencedirect.com/science/article/pii/S0012821X11002366 doi: https://doi.org/10.1016/j.epsl.2011.04.020

Woitischek, J., Woods, A. W., Edmonds, M., Oppenheimer, C., Aiuppa, A., Pering, T. D., et al. (2020). Strombolian eruptions and dynamics of magma degassing at Yasur Volcano (Vanuatu). *Journal of Volcanology and Geothermal Research*, *398*, 106869.

Xue, J.-Z., Herbolzheimer, E., Rutgers, M., Russel, W., & Chaikin, P. (1992). Diffusion, dispersion, and settling of hard spheres. *Physical review letters*, *69*(11), 1715.

Yoshimura, S. (2015). Diffusive fractionation of H_2O and CO_2 during magma degassing. *Chemical Geology*, *411*, 172 - 181. Retrieved from http://www.sciencedirect.com/science/article/pii/S0009254115003228 doi: https://doi.org/10.1016/j.chemgeo.2015.07.003

Zhang, Y., & Stolper, E. M. (1991). Water diffusion in a basaltic melt. *Nature*, *351*(6324), 306-309. Retrieved from https://doi.org/10.1038/351306a0 doi: 10.1038/351306a0